Q. J. R. Meteorol. Soc. (2001), **127**, pp. 2559–2597

Sensitivity of a heavy-rain-producing western Mediterranean cyclone to embedded potential-vorticity anomalies

By R. ROMERO*

NOAA/ National Severe Storms Laboratory, USA

(Received 13 December 2000; revised 5 July 2001)

SUMMARY

The development and track of a surface cyclone that produced heavy precipitation in the western Mediterranean region on 28–29 September 1994 is numerically simulated using a mesoscale model. Diagnostic calculations reveal that surface-pressure falls—and upward motion—occur in response to a well-defined pattern of upward quasi-geostrophic forcing at all tropospheric levels. In addition, convective instability and low-tropospheric water vapour flux convergence are significant over the western Mediterranean, and therefore the environment is highly supportive for convection development.

The appreciable dynamical forcing at upper levels appears to be associated with two positive potential-vorticity (PV) anomalies that are embedded within the large-scale trough and rotate about each other. Motivated by the fact that the small-scale features of the PV field are more prone to analysis or forecast error than the large-scale components, a sensitivity study is conducted in order to analyse the dependence of the mesoscale forecast on the initial intensity and position of the two embedded PV centres. This is accomplished by first applying a piecewise PV-inversion technique which allows the balanced flow associated with each PV centre to be calculated, and then the inverted mass and wind fields are used to modify the model initial conditions. Eight simulations are run after doubling or removing one or both anomalies (sensitivity to intensity), and eight other simulations after displacing the anomalies towards or away from the Iberian peninsula (sensitivity to position).

The results exhibit a clear dependence of the track and shape of the surface cyclone and its associated pattern of low-tropospheric warm air advection on the characteristics of the PV anomalies. Therefore, spatial details of the mesoscale forecast are shown to be highly sensitive to the precise structure of the upper-level dynamic forcing. Nevertheless, for the full set of arbitrarily defined initial conditions, one or several low pressure systems develop in the western Mediterranean area and heavy precipitation always occurs. On the other hand, there is an overall tendency of the simulations to favour cyclone development leeward of the Atlas mountain range and local rainfall enhancements over the exposed mountains of eastern Spain. The relative roles of the orography and sea surface latent-heat flux versus the action of the upper-level PV centres are examined by means of additional simulations.

KEYWORDS: Heavy rain Potential-vorticity inversion

1. INTRODUCTION

The genesis of heavy precipitation is a major meteorological threat in the western Mediterranean region (depicted in Fig. 1), especially during the late summer and autumn as a consequence of intense latent- and sensible-heat fluxes into the boundary layer from the warm Mediterranean sea. Resulting flash floods are relatively common, and catastrophic events for human life and property are recorded almost every year somewhere in eastern Spain, southern France, Italy or northern Africa. Some notable examples are the floods in Piedmont (Italy) on 5–6 November 1994 (maximum rainfall exceeded 300 mm in 24 h; Lionetti 1996), the flash flood in Vaison-La-Romaine (France) on 22 September 1992 (300 mm in 24 h; Sénési *et al.* 1996) and the Spanish flash floods in central Valencia on 3–4 November 1987 (800 mm in 24 h; Riosalido *et al.* 1988) and in south Catalonia on 9–10 October 1994 (up to 450 mm during the whole event; Wheeler 1995).

The strong social and economic impact of these events has motivated numerous observational, diagnostic and numerical modelling research efforts during the last two decades (e.g. the Mesoscale Alpine Programme; Binder and Schär 1998). Observations suggest that most of the flash flood events are associated with mesoscale convective

* Present affiliation: Dept. de Fisica, Universitat de les Illes Balears, 07071 Palma de Mallorca, Spain. e-mail: romu.romero@uib.es

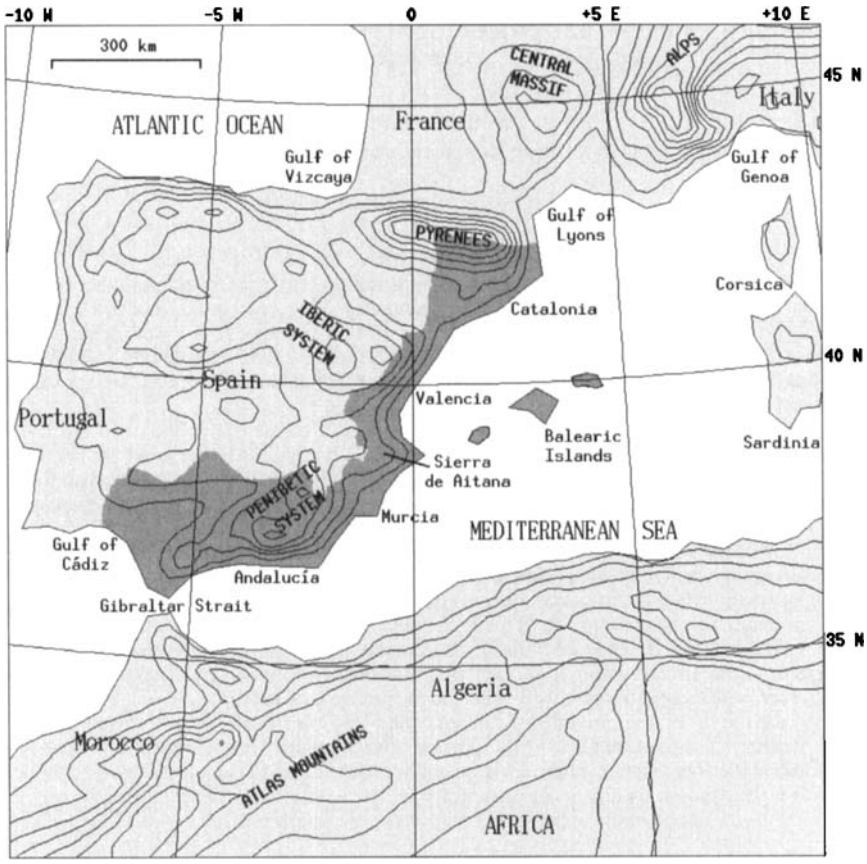

Figure 1. Depiction of the western Mediterranean region, with an indication of geographical locations and mountain systems mentioned in the text. Smoothed orography is contoured at 250 m intervals, starting at 250 m.

systems (e.g. Riosalido 1990), many of them triggered or enhanced by the coastal orographic features. Diagnostic studies (e.g. García-Dana *et al.* 1982; Ramis *et al.* 1994 and Doswell *et al.* 1998) have evaluated synoptic-scale processes and environmental parameters associated with the development of deep, moist convection, such as quasi-geostrophic forcing for upward motion, low-level moisture convergence and convective or latent instabilities (Doswell 1987). They have also inferred mesoscale lifting mechanisms responsible for the convection release and localization, typically associated with the interaction of the synoptic-scale flow with the complex orography of the region (see Fig. 1). Numerical modelling studies have been carried out to assess the predictability of these events (e.g. Fernández *et al.* 1995; Sénési *et al.* 1996) and, very importantly, have explored in detail the synoptic and mesoscale processes associated with the development and organization of the convection.

In particular, several authors have taken advantage of the potential offered by mesoscale models, and have isolated the role played by different physical factors by means of sensitivity or factor-separation techniques (Stein and Alpert 1993). Factors typically considered include the so-called boundary factors, such as local and remote orographies, surface characteristics and surface heat fluxes (e.g. Fernández *et al.* 1997; Ramis *et al.* 1998), together with others associated with the model physics, such as latent-heat exchanges in the parametrized moist processes (Buzzi *et al.* 1998; Romero

et al. 2000). Comparatively less attention, however, has been paid to the effects of internal features of the flow dynamics (jet streaks, troughs, fronts, etc.) probably because, unlike the external or parametrization factors, modifying or switching off these elements in the simulations is not straightforward. The three-dimensional nature, and the mutual dependence of pressure, temperature and wind fields pose serious constraints on the ways these fields can be altered without compromising the delicate dynamical balances that govern both the model and the actual fields.

A relatively simple approach to deal with internal dynamical features is based on the concept of potential vorticity (PV) and its invertibility principle (Hoskins *et al.* 1985 and references therein). According to this principle, given some balanced-flow constraints and proper boundary conditions for the meteorological fields (pressure, temperature and wind), the knowledge of the three-dimensional distribution of PV can be used to infer the balanced meteorological fields. Application of piecewise PV inversion is particularly useful since, once identified, any PV element of interest as well as its associated mass and wind fields can be isolated in a consistent way for diagnostic or prognostic purposes. Numerous studies have applied piecewise PV-inversion methods to diagnose, for example, the contributions and interactions of different PV anomalies for cases of surface cyclogenesis (e.g. Davis 1992a; Hakim *et al.* 1996; Huo *et al.* 1999a; Fehlmann and Davies 1999) and frontogenesis (e.g. Morgan 1999). But piecewise inversion schemes have also been applied for initial-value problems, where the effects on the subsequent forecast of incorporating, modifying or removing PV perturbations (i.e. a certain amount of balanced flow) in the model initial conditions are investigated. For example, Fehlmann *et al.* (2000) identify distinct mesoscale elements of the upper-level PV filament responsible for an Alpine rainstorm, and study the sensitivity of the forecast rainfall to these elements. Huo *et al.* (1999b) investigate the influence of the PV anomalies associated with two upper-level short-wave troughs on the numerical prediction of the March 1993 superstorm in the eastern USA. Huo *et al.* (1998) show that the forecast of that same explosive cyclogenesis event would have been improved by incorporating in the model initial conditions the PV anomaly associated with the surface temperature errors observed over oceanic regions.

In this work, the PV approach is used to investigate the sensitivity of a western Mediterranean cyclone, that produced heavy rain in eastern Spain, to the structure of the upper-level flow. The event took place on 28–29 September 1994, and was characterized by the development of several mesoscale convective systems (MCSs) over the western Mediterranean waters and the eastern part of Spain (Fig. 2). The MCSs affected mainly the southern and central parts of these areas during 28 September (Fig. 2(a)) but, as the low pressure system moved and expanded northwards the most important convection during 29 September developed in the northern part of the region (Fig. 2(b)). An analysis of the observed rainfall in eastern Spain during the episode (Fig. 3) exhibits significant amounts near the coasts, with the most important maxima in Valencia north of the Sierra de Aitana, the Balearic Islands, and north-eastern Catalonia. Serious damage in some agricultural and tourist areas was produced as a consequence of local floods.

Homar *et al.* (1999) present a diagnostic study and numerical simulation of this heavy precipitation event. They conclude that the evolution of the low pressure system and the associated convection was largely controlled, at synoptic scale, by a combination of warm and moist easterly advection at low tropospheric levels, typically observed in the flash flood events of the region, with less common strong and well-defined upper-level dynamical forcing (see also next section). The fact that the most intense convection evolved over the sea (Fig. 2) suggests, indeed, that quasi-geostrophic forcing for upward motion was particularly strong.

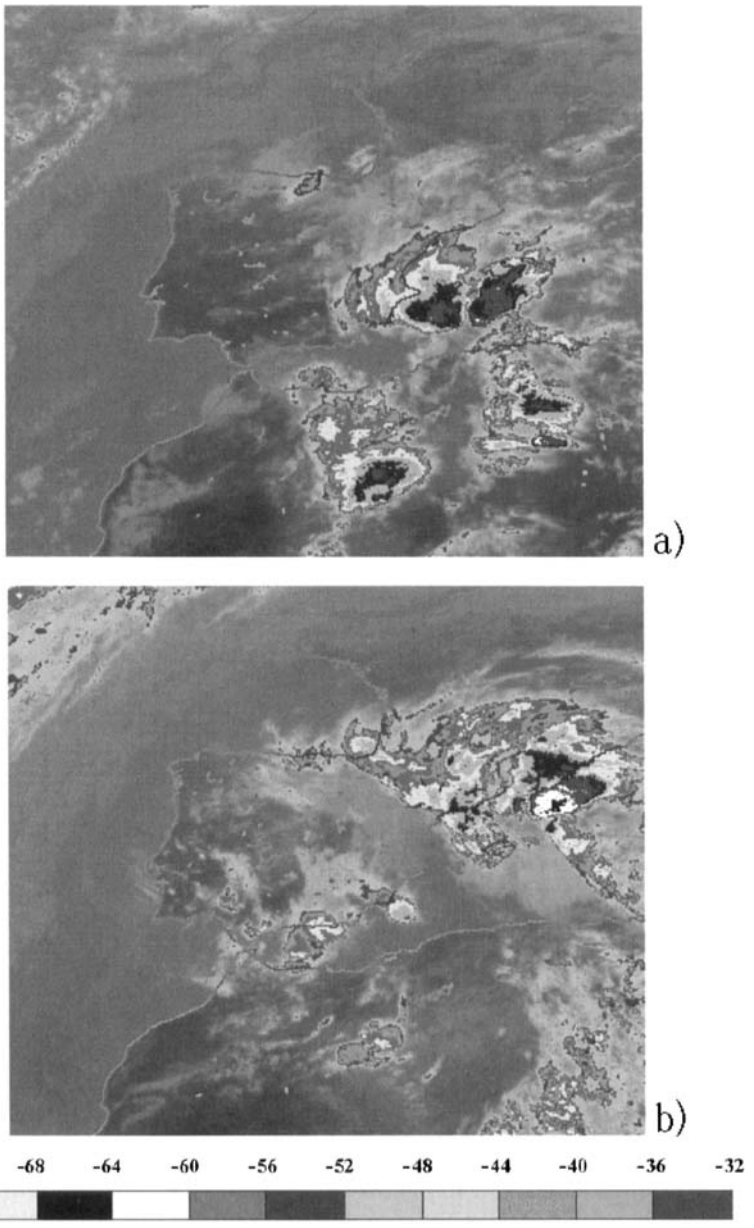

Figure 2. Infrared Meteosat pictures at (a) 12 UTC 28 September 1994, (b) 12 UTC 29 September 1994. Enhanced grey scales indicate cloud-top temperatures (°C) according to the key.

The focus of the present study is to investigate in more detail the role played by the upper-tropospheric disturbance, as described by its PV field, in the evolution of the event. Motivation for the study derives from a control numerical simulation and diagnostic products presented in next section, which show that the upper-level PV field upstream of the western Mediterranean was dominated by two PV centres rotating cyclonically about each other. Using a piecewise PV-inversion methodology, section 3 examines the sensitivity of the simulation to these PV centres by varying their intensity

Figure 3. Analysis of the observed 48 h rainfall (mm) in Mediterranean Spain (dark shaded region in Fig. 1) from 07 UTC 28 September 1994 to 07 UTC 30 September 1994.

and position in the model initial conditions. The conclusions from this sensitivity study and implications for forecasting this type of situation are contained in section 4.

2. NUMERICAL SIMULATION OF THE EVENT AND DISCUSSION

The 28–29 September 1994 heavy-precipitation event was numerically simulated using the non-hydrostatic version of the Pennsylvania State University–National Center for Atmospheric Research mesoscale model (Dudhia 1993; Grell *et al.* 1995). The model is formulated using the terrain-following sigma coordinate system, with enhanced vertical resolution in the boundary layer to better represent the turbulent processes. The model allows multiple-nest simulations with two-way interaction between successive nesting levels following the procedure devised by Zhang *et al.* (1986). In the present case, two interacting domains were used (those shown in Fig. 4). The coarse- and fine-grid domains are both centred at the same point on the coast of Valencia (0°W, 39°N) under a Lambert conformal map projection, and comprise 31 vertical sigma levels. In the horizontal, they have the same number of grid points (82 × 82), and resolutions of 60 and 20 km, respectively. The simulation presented covers 48 h, starting at 00 UTC 28 September 1994.

Initial and boundary conditions for the coarse-grid domain were based on a first guess provided by the global analyses from the National Centers for Environmental Prediction (NCEP) available at 00 and 12 UTC on standard isobaric surfaces. These meteorological analyses were interpolated horizontally to the model grid points, and improved using surface and upper-air observations with a successive-correction objective analysis technique (Benjamin and Seaman 1985). The resulting fields were then interpolated to the model sigma levels from the isobaric surfaces. Imbalances present in the data, generated during the interpolation process, were reduced by removing the

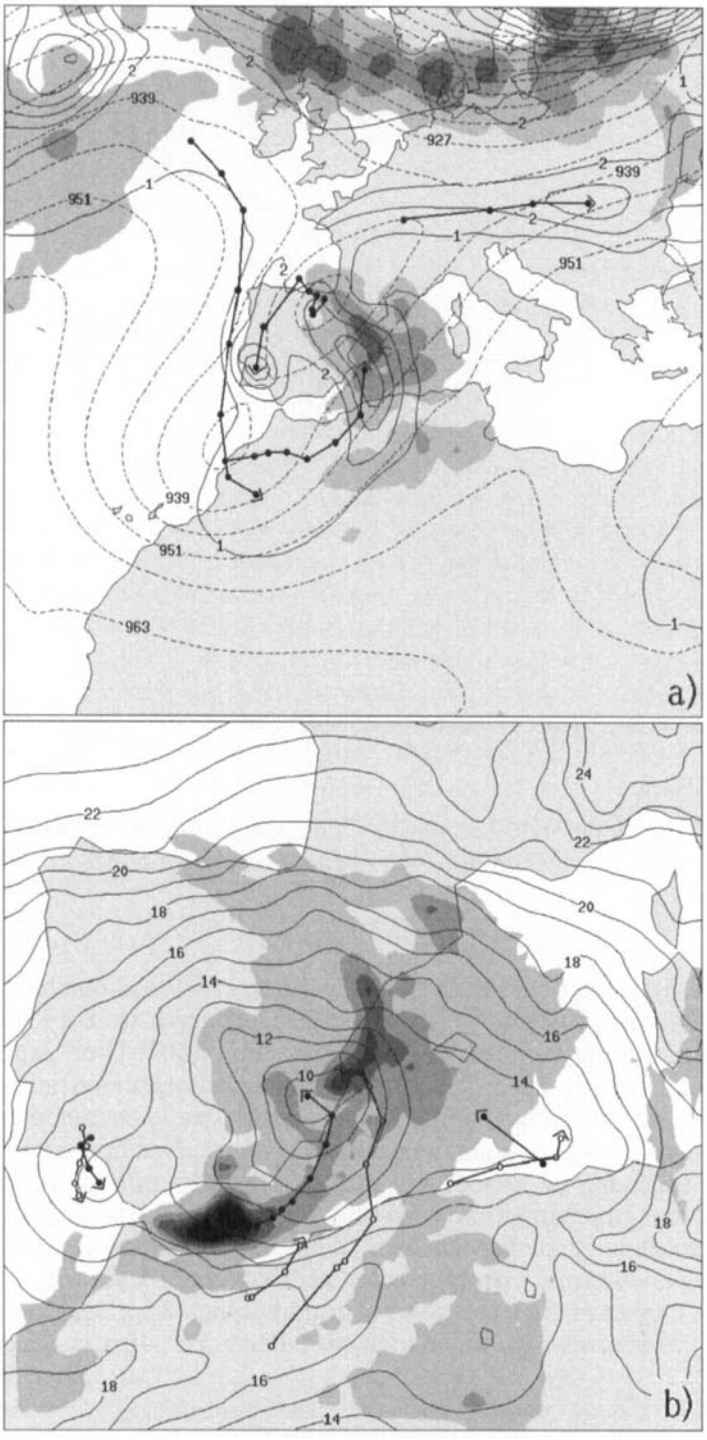

Figure 4. Control simulation *S*. (a) Geopotential height at 300 hPa at 06 UTC 28 September 1994 (dashed line; dam); Ertel's potential vorticity on the 330 K isentropic surface at 00 UTC 30 September 1994 (continuous line; PVU), with an indication of trajectories at 6 h intervals of several maxima present at that time (circles); and maximum value of the low tropospheric (1000–700 hPa) temperature advection observed during the simulation (shaded, for values exceeding 0.2, 0.4 and 0.6 K h^{-1}). (b) Mean-sea-level pressure at 00 UTC 30 September 1994 (continuous line; hPa but without the leading 1), with an indication of back trajectories at 3 h intervals of several minima (circles, with open circles for minima dissipated before that time); and total precipitation (shaded, for values exceeding 10, 40, 70, 100 and 130 mm).

vertical integral of the horizontal wind divergence at each model grid point (Washington and Baumhefner 1975). The initialization process was completed with horizontal interpolation of the coarse-grid fields to the fine grid. The tendencies along the model coarse-domain boundaries, expressed by differences of the boundary data at 12 h intervals, were applied using a Newtonian relaxation approach (Grell *et al.* 1995).

The Betts–Miller parametrization scheme (Betts 1986; Betts and Miller 1986) was chosen to calculate moist convection effects on the coarse-grid domain, whereas parametrized convection for the fine-grid domain followed the Kain–Fritsch scheme (Kain and Fritsch 1990). All the other physical parametrization schemes were identical for both domains. Explicit microphysics was represented, with predictive equations for cloud water and rainwater below the freezing level and cloud ice and snow above the freezing level (Dudhia 1989), including the effects of hydrostatic water loading, condensation, evaporation, melting, freezing, deposition and sublimation (Zhang 1989). The parametrization scheme used to represent the planetary boundary-layer physics was a modified version of the Blackadar (1979) scheme (Zhang and Anthes 1982; Zhang and Fritsch 1986). Surface temperature over land was calculated using a force-restore slab model (Blackadar 1979; Zhang and Anthes 1982), and over the sea remained constant during the simulation. Surface fluxes, as well as atmospheric temperature tendencies caused by long-wave and short-wave radiation components, were calculated taking into account the cloud cover (Benjamin 1983).

For the sake of brevity, the most relevant results of this simulation, referred to as control simulation S, are summarized in a single composite chart for both the synoptic scale (Fig. 4(a)) and mesoscale (Fig. 4(b)). As shown in Fig. 4(a), the upper-level flow at the beginning of the event was characterized by a positively tilted long-wave trough with its axis crossing the Iberian Peninsula. The induced flow over the western Mediterranean area at upper levels was thus from the south-west. Note, however, the complex structure of the upper-level wave, since, embedded within the large-scale trough there are two geopotential height minima, centred near the Gulf of Vizcaya and the Moroccan Atlantic coast (refer to Fig. 1 for locations). Calculation of Ertel's PV (Rossby 1940; Ertel 1942), defined as

$$q = \frac{1}{\rho}\eta \cdot \nabla\theta, \tag{1}$$

where ρ is the density, η the absolute vorticity vector and θ the potential temperature, reveals that the two embedded lows are each associated with a PV maximum, as expected. Figure 4(a)* displays the trajectories of these PV centres on the 330 K isentropic surface during the simulation, as well as their structure and position at the end of the period. Since both diffusion and diabatic effects are active in the model, neither the PV nor the potential temperature are conserved, but the use of isentropic—and even isobaric—PV charts aloft, where the above processes are relatively weak, allows an easy identification and tracking of any PV structure. Observe that, while rotating about each other, the PV centres initially located in the Gulf of Vizcaya and off the Moroccan coast migrate toward southern Portugal and the western Mediterranean, respectively. This movement implies high values of PV advection at upper levels over the western Mediterranean and eastern part of Spain, progressing from south to north (not shown). The overall cyclonic rotation and lifting of the upper-level trough is also reflected in the trajectories of other secondary PV structures, some of which are included in Fig. 4(a); for example, the PV centre associated with a short-wave trough initially located west of Ireland, which

* In this and subsequent figures PV is given in Potential Vorticity Units (PVU); 1 PVU = 10^{-6} K m^{2}kg^{-1}s^{-1}.

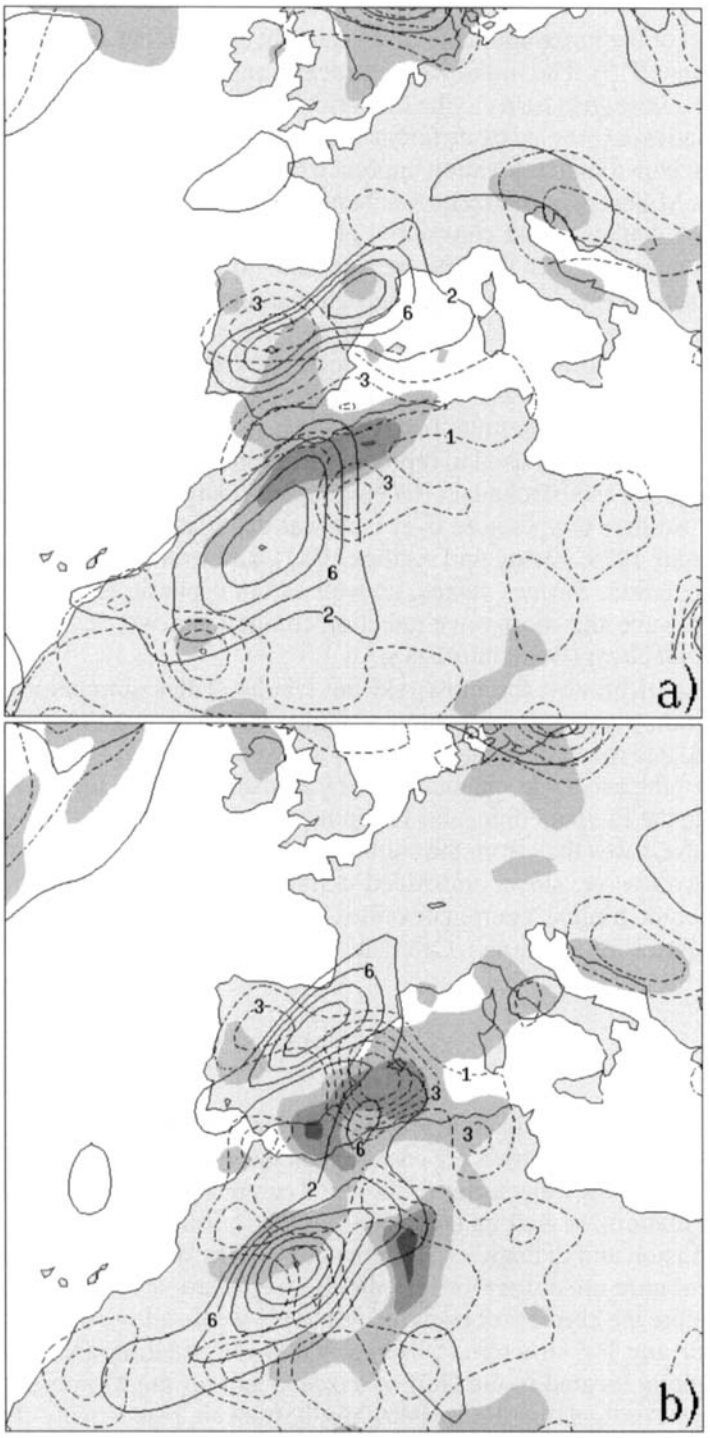

Figure 5. Time sequence for the control simulation *S* showing mid–upper tropospheric (700–200 hPa) upward quasi-geostrophic forcing (continuous line, starting at 2×10^{-18} m kg^{-1}s^{-1} every 4×10^{-18} m kg^{-1}s^{-1}); low tropospheric (1000–700 hPa) upward quasi-geostrophic forcing (dashed line, starting at 1×10^{-18} m kg^{-1}s^{-1} every 2×10^{-18} m kg^{-1}s^{-1}); and water vapour flux convergence in the layer 1000–700 hPa (shaded, for values exceeding 0.1, 0.5, 1 and 1.5 g m^{-2}s^{-1}): (a) at 12 UTC 28 September 1994, (b) at 00 UTC 29 September 1994, (c) at 12 UTC 29 September 1994, (d) at 00 UTC 30 September 1994. The quasi-geostrophic forcing is calculated following the *Q* vector formulation (Hoskins and Pedder 1980).

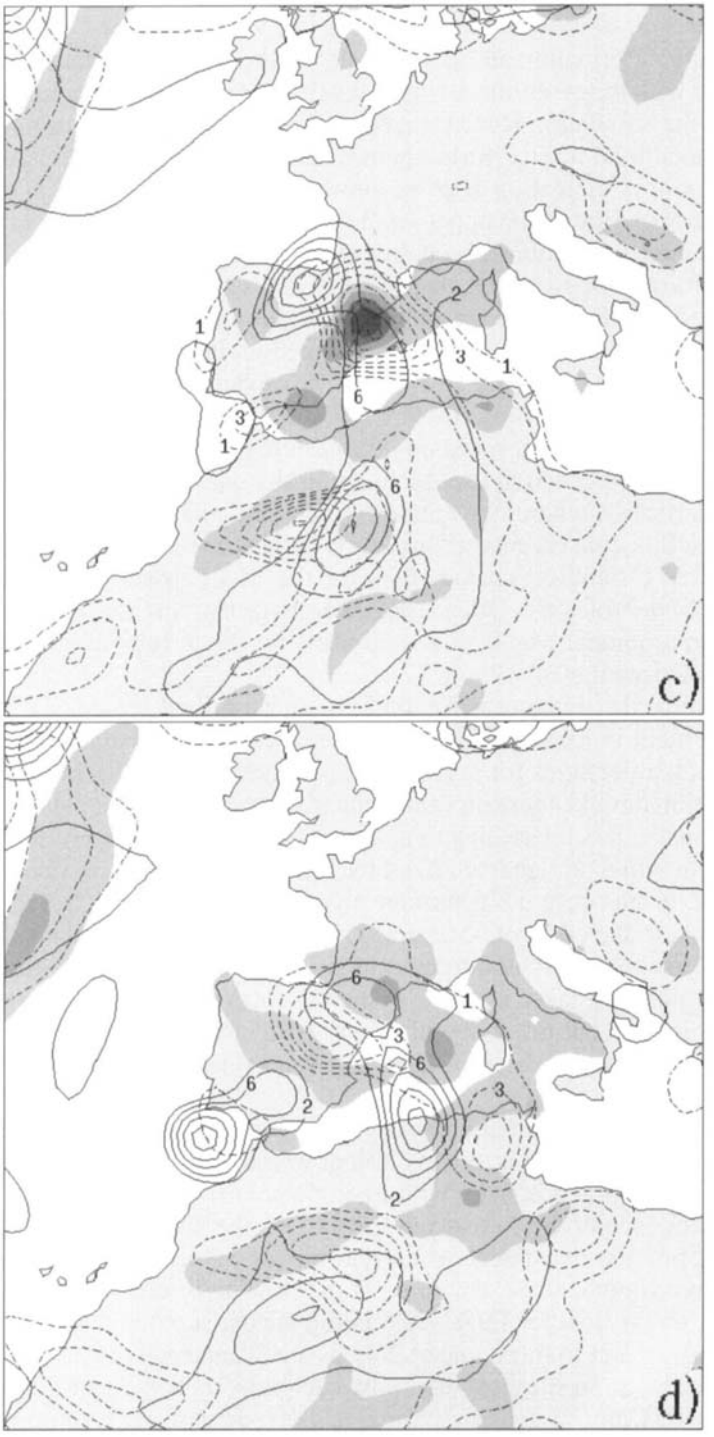

Figure 5. Continued.

progresses very rapidly southwards over the Atlantic and ends up in Morocco, or another centre first identified over northern France which moves eastwards. The latter is, in fact, the result of the split of the aforementioned main PV centre of the Gulf of Vizcaya after strong stretching deformation along the south-west to north-east direction.

Associated with the evolution at upper-levels, warm air advection in the lower troposphere during the simulation is maximized over the western Mediterranean and eastern Spain (see shaded field in Fig. 4(a)), again with the maximum of this field progressing from south to north. Calculation of quasi-geostrophic forcing for vertical motion (Fig. 5) reveals that the evolution of the upper-level PV and the low-level temperature advection fields are associated with important centres of dynamic forcing for upward motion in the mid-upper and lower troposphere, respectively. These areas of positive forcing tend to overlap the western Mediterranean and eastern Spain, and the overlapping zone moves northwards during 28–29 September, approximately following a cyclonic path along the Spanish Mediterranean coast (Fig. 5(a)–(d)). The model-predicted vertical velocity field (not shown) nearly replicates the structure found for the forcing, although the magnitude of the upward motion at low levels along the eastern coast of Spain is increasingly dominated by the orographic action (not included in the quasi-geostrophic formulation). In addition to a vertically coherent dynamic-forcing field, the model forecasts large values of water vapour flux convergence at low levels in the same areas (shaded field in Fig. 5). Since convective instability, characteristic of the Mediterranean air mass during the warm season (Meteorological Office 1962; Ramis 1995), was also present (not shown), the synoptic environment was highly supportive for the development and maintenance of convection (Doswell *et al.* 1996).

In response to the dynamical forcing pattern described previously, an intense cyclonic development is forecast over the western Mediterranean and Iberian peninsula (Fig. 4(b)). Back trajectories for several mean-sea-level pressure minima identified during the simulation have been incorporated into the figure to illustrate the evolution of the surface disturbance. It is interesting to note that, unlike many cases of flash flood events in eastern Spain which are characterized by relatively stationary surface lows near the Algerian coast, in this case the disturbance is mobile and progresses northwards from that genesis area to the coast of Valencia. This behaviour appears to be associated with the strong and evolving dynamic forcing identified aloft, whereas the former situations occur in dynamically weaker synoptic contexts, normally under a relatively stationary upper-level trough or cut-off low with its downstream section lying across the north African Atlas mountain range, thus favouring lee cyclogenesis along the Algerian coast (Romero *et al.* 2000).

Although the two embedded upper-level PV centres identified in Fig. 4(a) seem to be playing an important role in the evolution, intensity and areal extent of the surface cyclone, there is no practical way with a single control simulation of quantifying the degree of dependence of the mesoscale forecast on the specific structure of the upper-level flow. Despite the excellence of current numerical weather prediction systems in capturing many synoptic-scale structures of the flow up to several days in advance, the representation of the smaller large-scale components, such as the two embedded PV centres, may be subject to more uncertainty as a consequence of analysis and/or model errors. It would be interesting to learn how such uncertainty might affect a mesoscale forecast. With this aim, a sensitivity analysis of our case-study based on additional numerical simulations with perturbed initial conditions is carried out in the next section, similar to the strategy followed in Fehlmann *et al.* (2000). The object is to ascertain if the development and track of the surface cyclone, as well as its associated rainfall, are sensitive to the intensity and position of the upper-level PV centres.

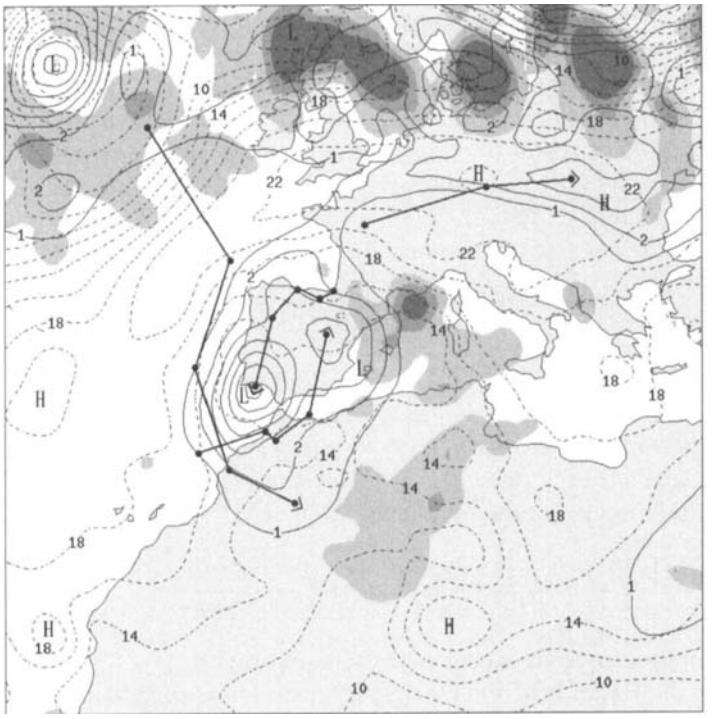

Figure 6. National Centers for Environmental Prediction analyses derived products: Ertel's potential vorticity on the 330 K isentropic surface at 00 UTC 30 September 1994 (continuous line; PVU), with an indication of trajectories at 12 h intervals of several maxima present at that time (circles); maximum value of the low tropospheric (1000–700 hPa) temperature advection observed during 00 UTC 28 September to 00 UTC 30 September 1994 (shaded, for values exceeding 0.2, 0.4 and 0.6 K h^{-1}); and mean-sea-level pressure at 00 UTC 30 September 1994 (dashed line; hPa but without the leading 10).

The forecast total precipitation by the control simulation *S* is displayed in Fig. 4(b). Though forecast accuracy is not necessary for the proposed sensitivity study, the skill of the model in capturing spatial and quantitative details of the rainfall field over Mediterranean Spain appears to be relatively high (compare with Fig. 3). The major deficiencies seem to occur over the sea; for example, the heavy precipitation centre predicted east of the Gibraltar strait is probably too strong, and the model seems to be incapable of developing the intense convection that occurred in the northern part of the Mediterranean (Fig. 2(b)) (a problem also observed in the simulation of the same event by Homar *et al.* (1999) for which a different model and initialization data were used). On the other hand, the dynamical evolution as simulated by the control experiment appears to be supported, in its gross features, by the information contained in the NCEP improved analyses (Fig. 6). Nevertheless, the rotation rate and intensity of the analysed upper-level PV anomalies are stronger than for the simulated anomalies, and there are other discrepancies in the structure of the mean-sea-level pressure and thermal advection fields (compare with Fig. 4).

3. SENSITIVITY TO THE UPPER-LEVEL PV CENTRES

The method used to explore the sensitivity of the mesoscale simulation to the upper-level PV centres, for convenience hereinafter referred to as SW PV and NE PV centres according to their initial geographical location (Fig. 4(a)), requires the calculation of a

balanced flow associated with each anomaly that can be used to alter the model initial conditions in a physically consistent way without introducing any significant noise. The piecewise PV-inversion technique of Davis and Emanuel (1991) was used for such purpose. The method starts with the calculation of the balanced flow, described by ϕ (geopotential) and ψ (stream function), from the total or instantaneous distribution of Ertel's PV q, given by (1). The balance assumption made herein follows the Charney (1955) nonlinear balance equation:

$$\nabla^2\phi = \nabla \cdot f\nabla\psi + 2m^2 \left\{ \frac{\partial^2}{\partial x^2}\frac{\partial^2\psi}{\partial y^2} - \left(\frac{\partial^2\psi}{\partial x \partial y}\right)^2 \right\}, \tag{2}$$

where f is the Coriolis parameter and m denotes the map-scale factor of the particular (x, y) projection used. The other diagnostic relation necessary for the inversion of ϕ and ψ is given by the approximate form of (1) resulting from the hydrostatic assumption and the same scale analysis used to derive (2), namely, that the irrotational component of the wind is very small relative to the nondivergent wind:

$$q = \frac{g\kappa\pi}{p}\left\{(f + m^2\nabla^2\psi)\frac{\partial^2\phi}{\partial\pi^2} - m^2\left(\frac{\partial^2\psi}{\partial x\partial\pi}\frac{\partial^2\phi}{\partial x\partial\pi} + \frac{\partial^2\psi}{\partial y\partial\pi}\frac{\partial^2\phi}{\partial y\partial\pi}\right)\right\}, \tag{3}$$

where p is the pressure, g the acceleration due to gravity, $\kappa = R_d/C_p$, and the vertical coordinate π is the Exner function $C_p(p/p_0)^\kappa$. (C_p is the specific heat of air at constant pressure, and R_d the gas constant for dry air.)

The finite-difference form of the closed system described by (2) and (3) is solved for the unknowns ϕ and ψ given q, using an iterative technique until convergence of the solutions is reached (see Davis and Emanuel 1991 for details). Neumann-type conditions ($\partial\phi/\partial\pi = f\partial\psi/\partial\pi = -\theta$) are applied on the top and bottom boundaries, and Dirichlet conditions on the lateral boundaries. The latter are supplied by the observed geopotential, and the stream function calculated by matching its gradient along the edge of each isobaric surface to the observed normal wind component, which is first slightly modified to force no net divergence in the domain. Because of the balance condition used, the inverted fields are very accurate even for meteorological systems characterized by large Rossby numbers (Davis and Emanuel 1991; Davis 1992b).

Next, a reference state must be found from which to define perturbations. As in Davis and Emanuel (1991), this reference state is defined as a time average. Given $\overline{q}$, the time mean of q, a balanced mean flow $(\overline{\phi}, \overline{\psi})$ is inverted from identical equations to (2) and (3), except that all dependent variables are mean values, and the mean potential temperature, $\overline{\theta}$, is used for the top and bottom boundary conditions. The perturbation fields (q', ϕ', ψ') are given by the definitions:

$$(q, \phi, \psi) = (\overline{q}, \overline{\phi}, \overline{\psi}) + (q', \phi', \psi'). \tag{4}$$

Finally, we can consider that the PV perturbation field q' is partitioned into N portions or anomalies, $q' = \sum_{n=1}^{N} q_n$. We are interested in obtaining that part of the flow (ϕ_n, ψ_n) associated with each PV portion q_n, and we also require $\phi' = \sum_{n=1}^{N}\phi_n$ and $\psi' = \sum_{n=1}^{N}\psi_n$. As discussed in Davis (1992b), there is no unique way to define a relationship between (ϕ_n, ψ_n) and q_n because of the nonlinearities present in (2) and (3). Here, we adopt the linear method of Davis and Emanuel (1991), derived after substitution of (4) and the above summations in (2) and (3) and equal partitioning of the nonlinear term among the other two linear terms that result from each nonlinearity in the above equations (see Davis and Emanuel 1991 for details). The resulting linear

closed system for the nth perturbation is:

$$\nabla^2\phi_n = \nabla \cdot f\nabla\psi_n + 2m^2\left(\frac{\partial^2\psi^*}{\partial x^2}\frac{\partial^2\psi_n}{\partial y^2} + \frac{\partial^2\psi^*}{\partial y^2}\frac{\partial^2\psi_n}{\partial x^2} - 2\frac{\partial^2\psi^*}{\partial x\partial y}\frac{\partial^2\psi_n}{\partial y\partial x}\right), \tag{5}$$

$$q_n = \frac{g\kappa\pi}{p}\left\{(f + m^2\nabla^2\psi^*)\frac{\partial^2\phi_n}{\partial\pi^2} + m^2\frac{\partial^2\phi^*}{\partial\pi^2}\nabla^2\psi_n - m^2\left(\frac{\partial^2\phi^*}{\partial x\partial\pi}\frac{\partial^2\psi_n}{\partial x\partial\pi} + \frac{\partial^2\phi^*}{\partial y\partial\pi}\frac{\partial^2\psi_n}{\partial y\partial\pi}\right) - m^2\left(\frac{\partial^2\psi^*}{\partial x\partial\pi}\frac{\partial^2\phi_n}{\partial x\partial\pi} + \frac{\partial^2\psi^*}{\partial y\partial\pi}\frac{\partial^2\phi_n}{\partial y\partial\pi}\right)\right\}, \tag{6}$$

where $()^* = \overline{()} + \frac{1}{2}()'$.

The system (5)–(6) is solved for each PV anomaly of interest. A portion θ_n of the perturbation potential temperature can be used for the top and bottom boundary conditions, whereas homogeneous boundary conditions for ϕ_n and ψ_n are normally assumed at the lateral boundaries for interior PV anomalies such as the ones considered.

(*a*) *Piecewise PV-inversion results and design of the simulations*

The piecewise PV-inversion scheme was applied to invert the SW and NE PV anomalies at 00 UTC 28 September 1994, the simulation start time. The inversion was performed using the NCEP-based isobaric analyses that were created for the model coarse domain (see section 2), placing the top and bottom boundaries at 100 and 1000 hPa, respectively. The perturbation PV field was defined as the departure from the six-day time average about 00 UTC 28 September, and the pieces representing the two anomalies were identified as the volumes of positive PV perturbation above 500 hPa present to the south-west and north-east of the Gulf of Cádiz. Figure 7(a) shows the structure of the SW and NE PV anomalies at 250 hPa, as well as the remainder of the total PV field at the same level without the anomalies. Deliberately, the selected reference or mean state is such that, even without the anomalies, the PV field is still characterized by the intrusion of a tongue of high PV towards the Iberian peninsula and lower latitudes. This is because we are interested in manipulating the two embedded upper-level lows that are shaping the large-scale trough (Fig. 4(a)), not the trough itself (represented by the high-PV tongue).

A plan view at 250 hPa of the inverted circulations is included in Fig. 7(b). The remainder of the flow without the balanced circulations of the anomalies, or background flow, is also shown in vector form. Clearly, the effect of the background flow is mainly to advect the SW PV anomaly towards the western Mediterranean and to stretch the NE PV anomaly along the south-west to north-east direction. The circulations associated with the anomalies are contributing to their self-rotation and to the cyclonic rotation—or negative tilting—of the main trough. To a lesser extent the anomalies are also contributing to advect each other along a cyclonic path. All these lateral interactions are consistent with the evolution of the upper-level flow observed in the control simulation (Fig. 4(a)), although the individual contributions displayed in Fig. 7(b) are only representative of the initial stage of the episode, and therefore, PV inversions for later times would be needed for a complete diagnosis of these evolving interactions.

A vertical cross-section of the inverted balanced fields (Fig. 8) illustrates that the localized PV anomalies are felt throughout the entire atmospheric column, a natural consequence of the Laplacian operators involved in the system of equations (5)–(6). Although the response, in the form of geopotential deficit, cyclonic circulation, and

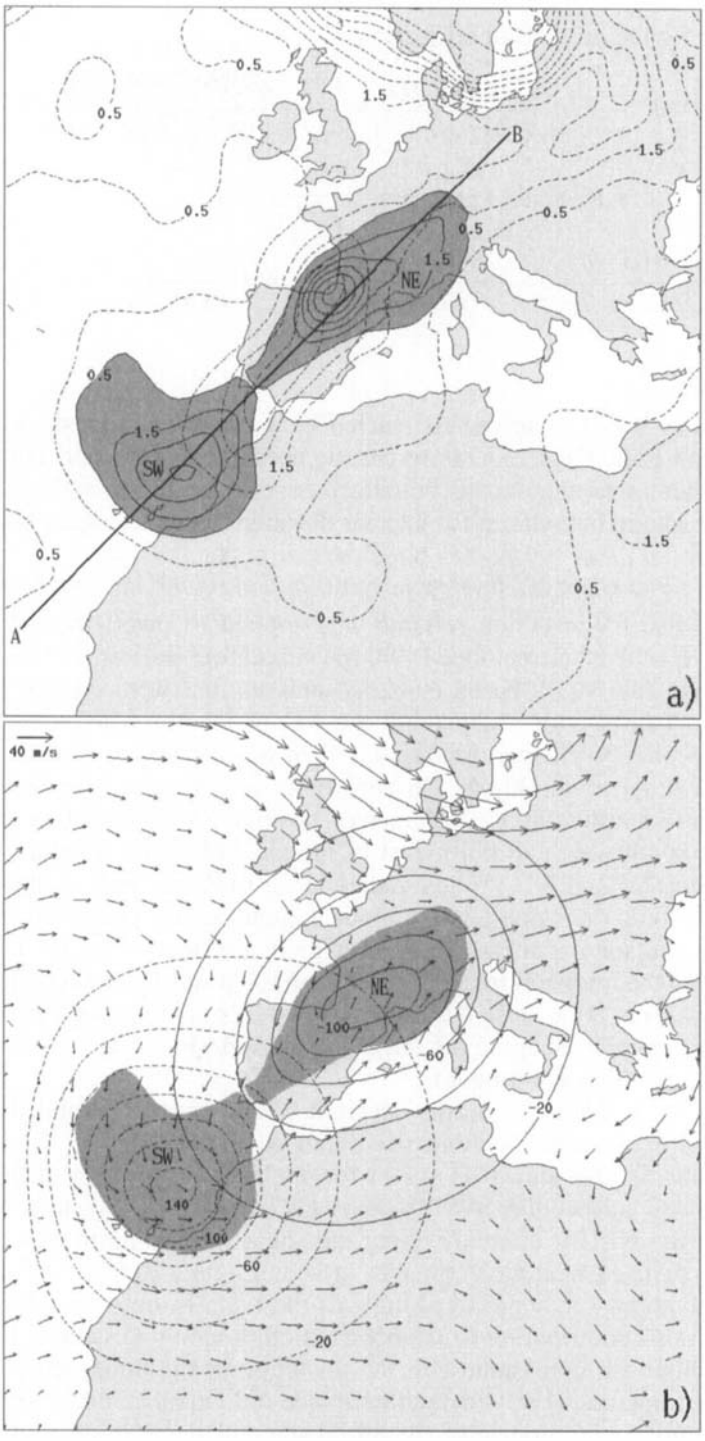

Figure 7. Piecewise potential vorticity (PV) inversion at 00 UTC 28 September 1994: (a) Ertel's PV at 250 hPa corresponding to the south-west (SW) and north-east (NE) anomalies (continuous line, starting at 0.5 PVU every 1 PVU) and the total field without the anomalies (dashed line, starting at 0.5 PVU every 1 PVU). (b) Stream function at 250 hPa of the balanced flow derived from the SW and NE PV anomalies (dashed and continuous line respectively, starting at -20×10^5 m^2s^{-1} every -20×10^5 m^2s^{-1}); and vector wind field at 250 hPa corresponding to the total flow without the balanced components associated with the anomalies (a reference vector is shown in the upper-left corner).

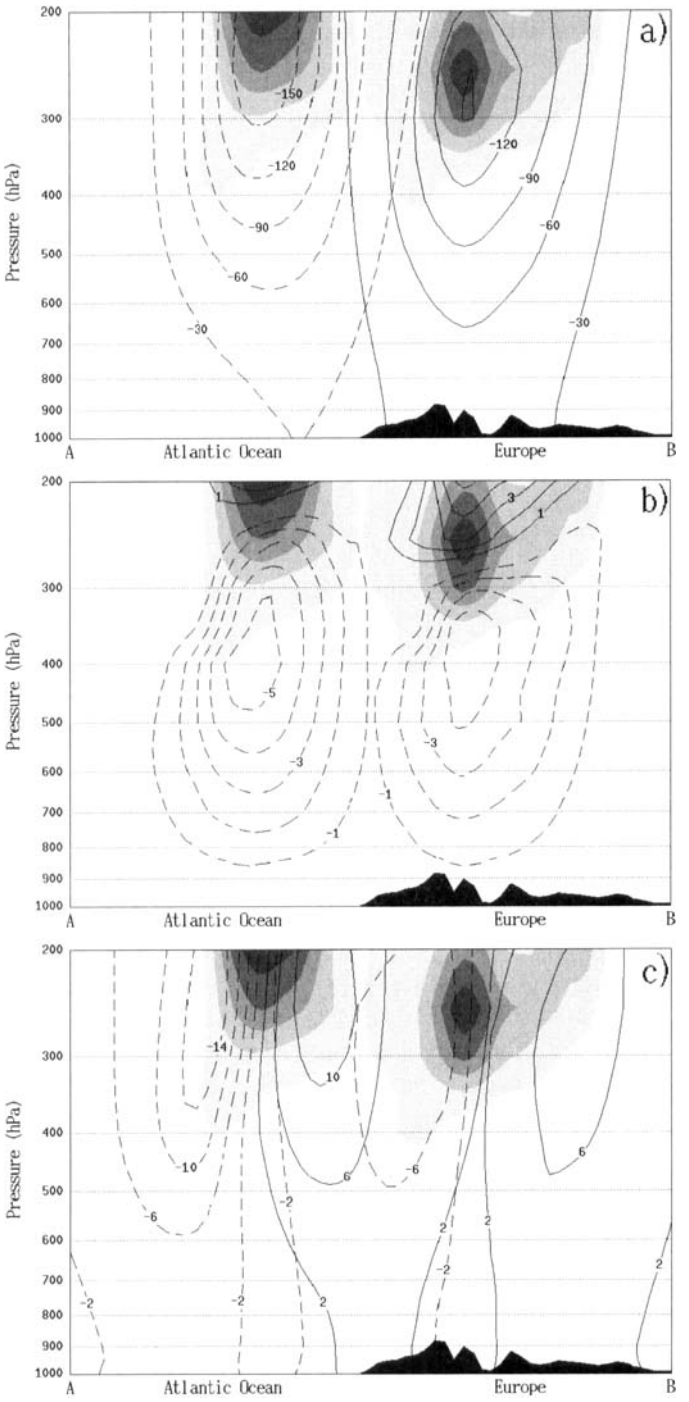

Figure 8. Vertical cross section along the line AB shown in Fig. 7(a) of the potential-vorticity (PV)-inverted fields from the south-west (SW) and north-east (NE) anomalies at 00 UTC 28 September 1994. (a) Geopotential height (dashed and continuous contours for the SW and NE anomalies, respectively, starting at −30 m every −30 m); (b) temperature (continuous line for positive values and dashed line for negative values, in 1 degC intervals starting at 1 and −1 °C, respectively); and (c) section-normal winds (continuous line for flow into the page and dashed line for flow out of the page, at 4 m s^{-1} intervals starting at 2 and −2 m s^{-1}, respectively). The SW and NE PV anomalies are shaded for values exceeding 0.5, 1.5, 2.5, 3.5 and 4.5 PVU.

TABLE 1. SUMMARY OF THE NUMERICAL EXPERIMENTS PERFORMED IN ORDER TO INVESTIGATE THE SENSITIVITY OF THE SIMULATION TO THE INTENSITY OF THE UPPER-LEVEL PV ANOMALIES

Experiment	South-west anomaly	North-east anomaly
S_0^0	Removed	Removed
S_2^2	Doubled	Doubled
S_1^0	Unchanged	Removed
S_2^0	Doubled	Removed
S_0^1	Removed	Unchanged
S_0^2	Removed	Doubled
S_2^1	Doubled	Unchanged
S_1^2	Unchanged	Doubled

TABLE 2. SUMMARY OF THE NUMERICAL EXPERIMENTS PERFORMED IN ORDER TO INVESTIGATE THE SENSITIVITY OF THE SIMULATION TO THE POSITION OF THE UPPER-LEVEL PV ANOMALIES

Experiment	South-west anomaly	North-east anomaly
S_-^-	Moved inwards	Moved inwards
S_+^+	Moved outwards	Moved outwards
$S_=^-$	Unchanged	Moved inwards
S_+^-	Moved outwards	Moved inwards
$S_-^=$	Moved inwards	Unchanged
S_-^+	Moved inwards	Moved outwards
$S_+^=$	Moved outwards	Unchanged
$S_=^+$	Unchanged	Moved outwards

cooling under the anomalies or warming above, is stronger at mid-upper levels, these effects are also felt in the lower troposphere. This emphasizes that a potential error in resolving the upper-level PV centres would be reflected not only at the anomaly level, but throughout the troposphere down to the surface, affecting key fields for surface cyclogenesis and forcing of vertical motion such as the temperature advection pattern.

The sensitivity experiments were designed by adding and/or subtracting the PV-inverted balanced fields (geopotential, temperature and wind) into the model initial conditions on the isobaric surfaces, previous to vertical interpolation to the model sigma levels. The relative-humidity field was kept unaltered. Two sets of simulations were designed to study separately the sensitivity of the forecast to the intensity and position of the anomalies (Tables 1 and 2, respectively). In the first set, the SW and NE PV anomalies are either doubled (adding the inverted fields), removed (subtracting the fields) or kept unchanged, entailing eight simulations in addition to the control run from all the possible combinations (summarized in Table 1). In the second set, the intensity of the anomalies is not changed but the position is shifted along the AB axis shown in Fig. 7(a). The anomalies are either moved outwards (by subtracting the associated fields and adding them 425 km farther from the Iberian peninsula), moved inwards (in the same way except 425 km closer to the Iberian peninsula) or kept in the original position, implying again eight additional simulations (Table 2). All these modified experiments were run with identical boundary conditions and physics options as the control run and for the same 48 h period.

Obviously, the above-mentioned ensemble of experiments is arbitrarily defined. On the other hand, no experiments were done with modified intensities and modified positions of the anomalies at the same time, in order to keep the number of simulations small. Nevertheless, as we will see in the next sections, the designed experiments appear to embrace a wide range of synoptic scenarios; these look similar from a broad perspective (since all share the presence of a well-defined trough upstream from the Mediterranean in agreement with the climatology of these situations), but contain differences that turn to be crucial for the mesoscale forecast and, therefore, peculiarities of the synoptic wave aloft cannot in general be ignored. The results of the 16 simulations are presented below.

(*b*) *Sensitivity to the intensity of the PV anomalies*

Experiment S_0^0 represents the null or basic case in which the anomalies have simply been eliminated. For easy comparison, the results (Fig. 9) are presented in the same format as the control experiment (Fig. 4). Note that in this case the upper-level flow pattern is evolving more slowly about the Iberian peninsula without the spinning PV centres (Fig. 9(a)). This is reflected in a nearly stationary trough that remains positively tilted during the whole episode. Quasi-geostrophic forcing for upward motion (not shown) is weaker at all levels over the area of interest and is mainly confined to the southern part of the Mediterranean. Observe, for example, that low-tropospheric warm advection is weaker than in the control simulation, and is only significant to the south of the Balearic Islands (compare Figs. 9(a) and 4(a)). The resulting surface low pressure area is not a mobile one and is less intense, remaining near the Algerian coast without exhibiting any significant northward extension throughout the episode (Fig. 9(b)). This scenario resembles many other situations (e.g. the 'Gandía' case in Romero *et al.* 2000) in which the lack of strong and evolving upper-level dynamic forcing implies near-stationary disturbances leeward of the Atlas mountains that locally enhance the easterly moist flow towards eastern Spain. Despite the 'weakness' of the S_0^0 situation, heavy precipitation is still produced, although mainly confined to southern Mediterranean waters (Fig. 9(b)).

Doubling the intensity of both PV centres (experiment S_2^2) amounts to increasing the rotation rate of the anomalies about each other, as clearly illustrated in the trajectories included in Fig. 10(a). Dynamic forcing for upward motion is also stronger and more mobile than in the control run. Intense warm advection at low levels is not restricted to the western Mediterranean region but also affects most of the central and northern Iberian peninsula. The strength of the S_2^2 pattern is reflected in a very broad low pressure area, with the main centre now located over western Spain at the end of the simulation, and the axis of the heavy precipitation is somewhat displaced inland (Fig. 10(b)).

Without the NE PV anomaly (experiment S_1^0), the SW PV anomaly is not advected as far into the western Mediterranean region, indicated by the fact that its path length (Fig. 11(a)) is approximately half of that in the control run. As a consequence, significant values of dynamic forcing and low-level warm advection occur in the southern and central parts of the region but not in its northern part. Consistently, the surface low-pressure area is not very mobile and does not embrace the northern part of the region; Catalonia and the northern Mediterranean are free of any significant rainfall (Fig. 11(b)).

If the SW PV anomaly is doubled (S_2^0), its self-rotation is increased and the centre of the anomaly now moves into southern Spain during the episode (not shown). Owing to the enhanced intensity of the upper-level southern low, quasi-geostrophic upward forcing aloft is more intense than in the previous case, and low-tropospheric warm

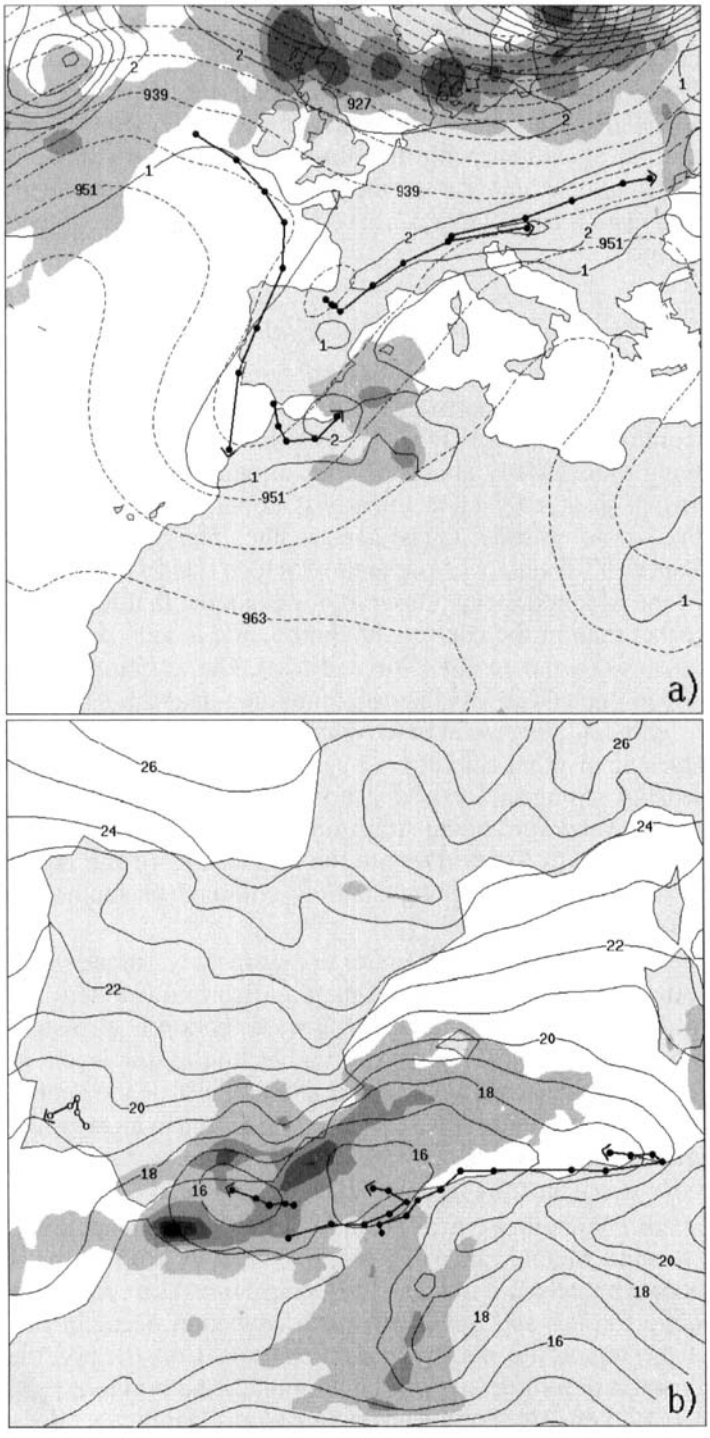

Figure 9. As Fig. 4, but for experiment S_0^0.

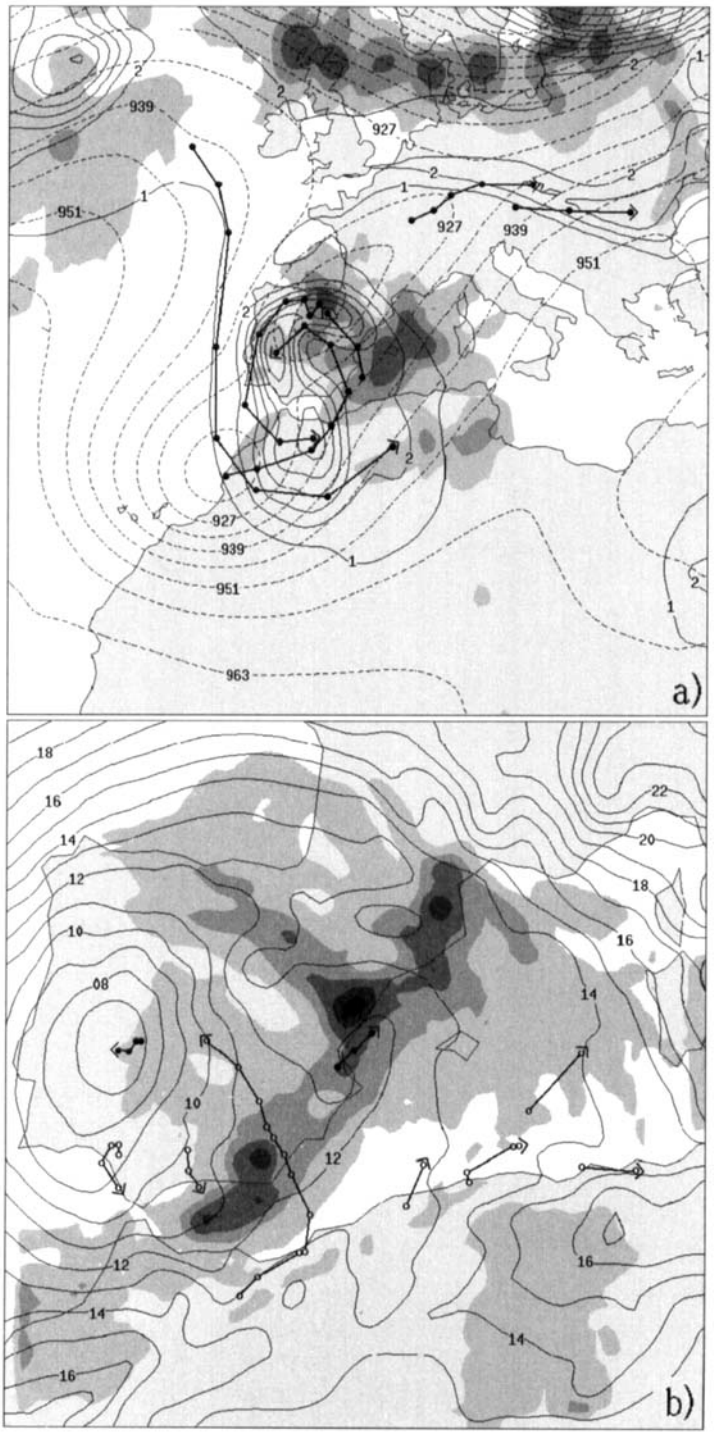

Figure 10. As Fig. 4, but for experiment S_2^2.

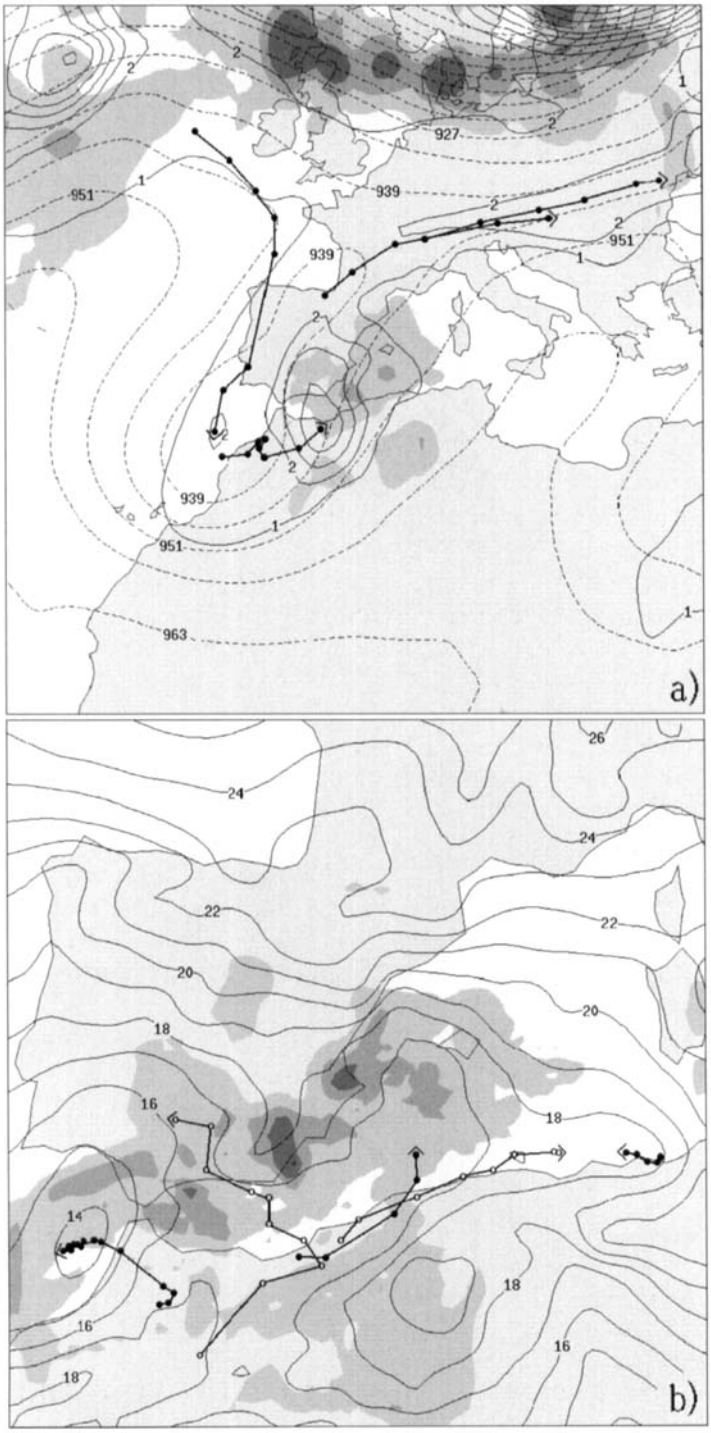

Figure 11. As Fig. 4, but for experiment S_1^0.

advection values are also a bit higher. Interestingly, both the surface pressure pattern and the rainfall distribution (not shown) are very similar to the previous result, although the surface depressions are somewhat deeper and the precipitation more widespread in this case.

As expected, the lack of the SW PV anomaly (simulation S_0^1) is noted in reduced translation of the NE PV anomaly compared with the control run (Fig. 12(a)). The S_0^1 case is qualitatively different to the previous ones in that the pattern of warm advection in the lower troposphere is concentrated to the east and north of the Balearic Islands (see shaded field in Fig. 12(a)). The greatest surface pressure falls occur along the western part of this pattern, where there is also a contribution from the upper-level forcing induced downstream of the NE PV anomaly. The resulting low pressure centre is intense and exhibits a long track over the Mediterranean, with most of the heavy rainfall being produced over oceanic areas and north-east Spain (Fig. 12(b)).

When the NE PV anomaly is doubled (experiment S_0^2), the dynamic-forcing field is stronger, especially at upper levels, and evolves more rapidly. The pattern of appreciable warm air advection at low levels describes a cyclonic trajectory during the episode and, in contrast with the previous case, progresses well into northern Spain (Fig. 13(a)). The surface disturbance follows a similar trajectory to the previous situation, S_0^1, but, since it moves faster, by the end of the period the pressure minimum is located over central Spain and the area of relative low pressure is very broad, encompassing the whole western Mediterranean and most of the Iberian peninsula (Fig. 13(b)). Following the track of the surface disturbance, the forecast precipitation field is similar to the previous one, except it is generally less intense and more spread over the sea and extends farther into northern Spain.

The evolution of the upper-level PV field and the corresponding dynamic forcing for upward motion are also intensified by maintaining the NE PV anomaly but doubling the SW PV anomaly (experiment S_2^1). The structure of the low-tropospheric warm air advection—and therefore of the quasi-geostrophic dynamic forcing at low levels—during the simulation is similar to the control run, but with higher values in the west of the region around Gibraltar strait. In fact, the surface pressure pattern and the accumulated rainfall field are relatively similar in both runs. However, in the present case more rainfall is generated in western regions of Spain and the main low pressure minimum evolves near Gibraltar strait (not shown).

The outcome of the reverse situation, S_1^2, in which the SW PV anomaly is unchanged and the NE PV anomaly is doubled, turns out to be very similar to the forecast by experiment S_0^2, although the precipitation is generally greater in the present case.

(c) *Sensitivity to the position of the PV anomalies*

The effect of bringing the SW and NE PV anomalies together (experiment S_-^-) can be seen as a situation in which the upper-level PV field is characterized by a single, big PV centre. While rotating very quickly about itself, this centre describes a cyclonic trajectory around the Gibraltar strait during the simulation period (Fig. 14(a)). The mesoscale forecast in this situation (Fig. 14(b)) is almost identical to the results of experiment S_2^1. This is interesting, since the initial upper-level flow patterns differ substantially. Calculation of quasi-geostrophic forcing for upward motion reveals, however, that the magnitude and spatial pattern of the forcing field at low and mid-upper levels are similar in both cases (not shown).

When the two PV anomalies are moved away from the Iberian peninsula (experiment S_+^+), the coupling between the SW and NE disturbances is weakened. The result is

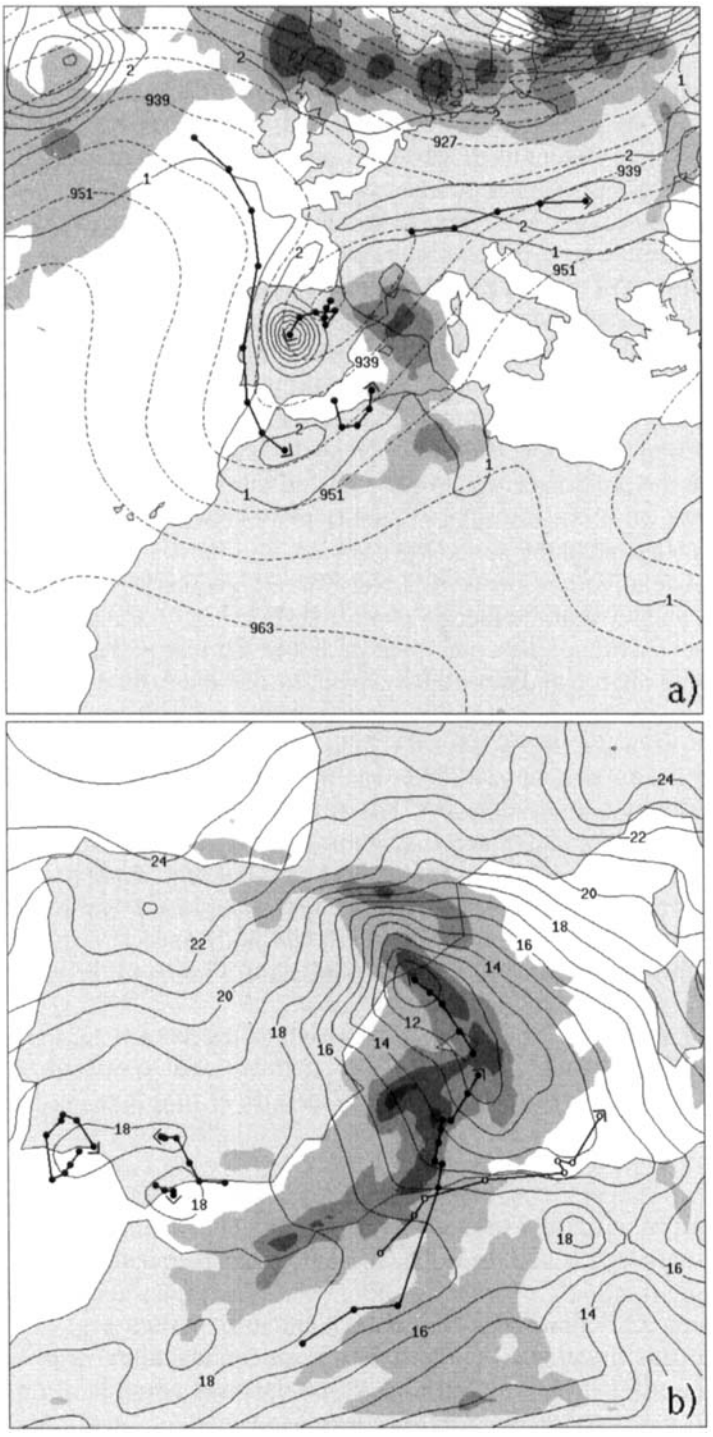

Figure 12. As Fig. 4, but for experiment S_0^1.

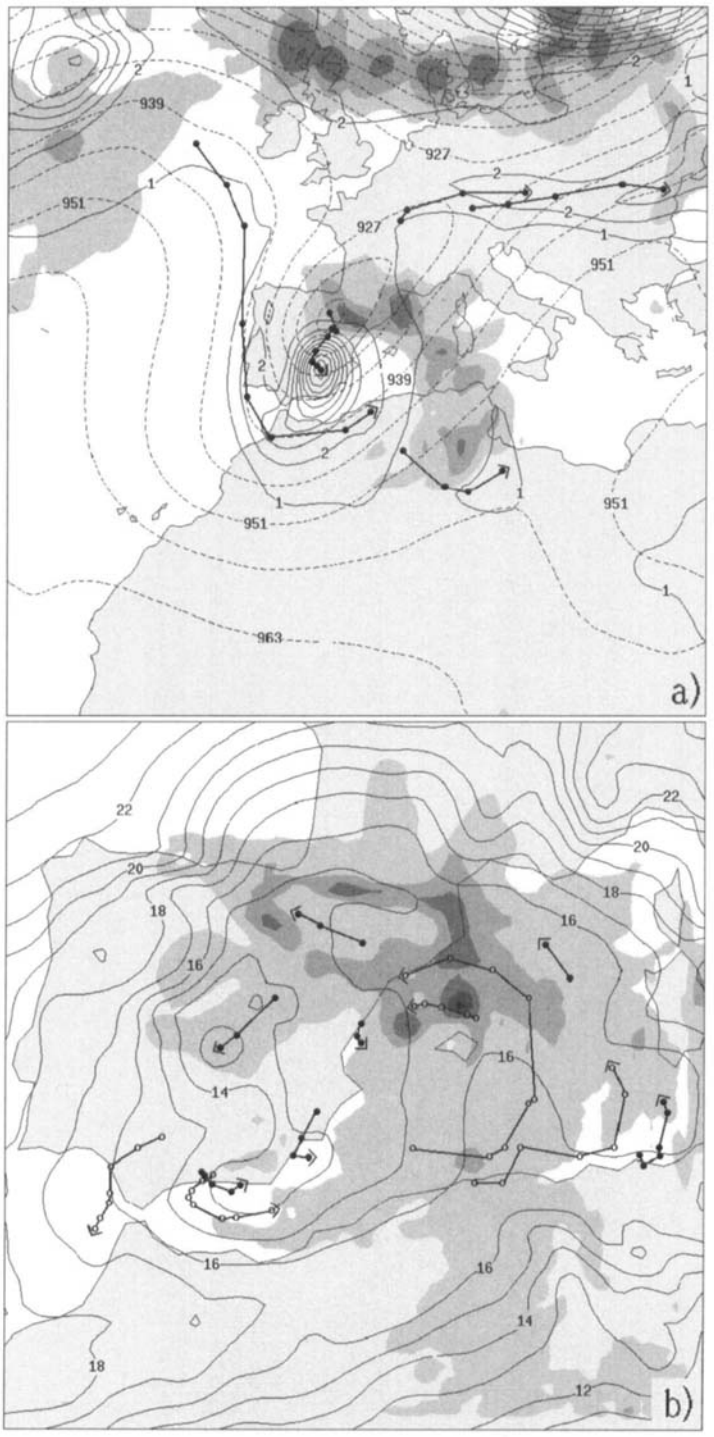

Figure 13. As Fig. 4, but for experiment S_0^2.

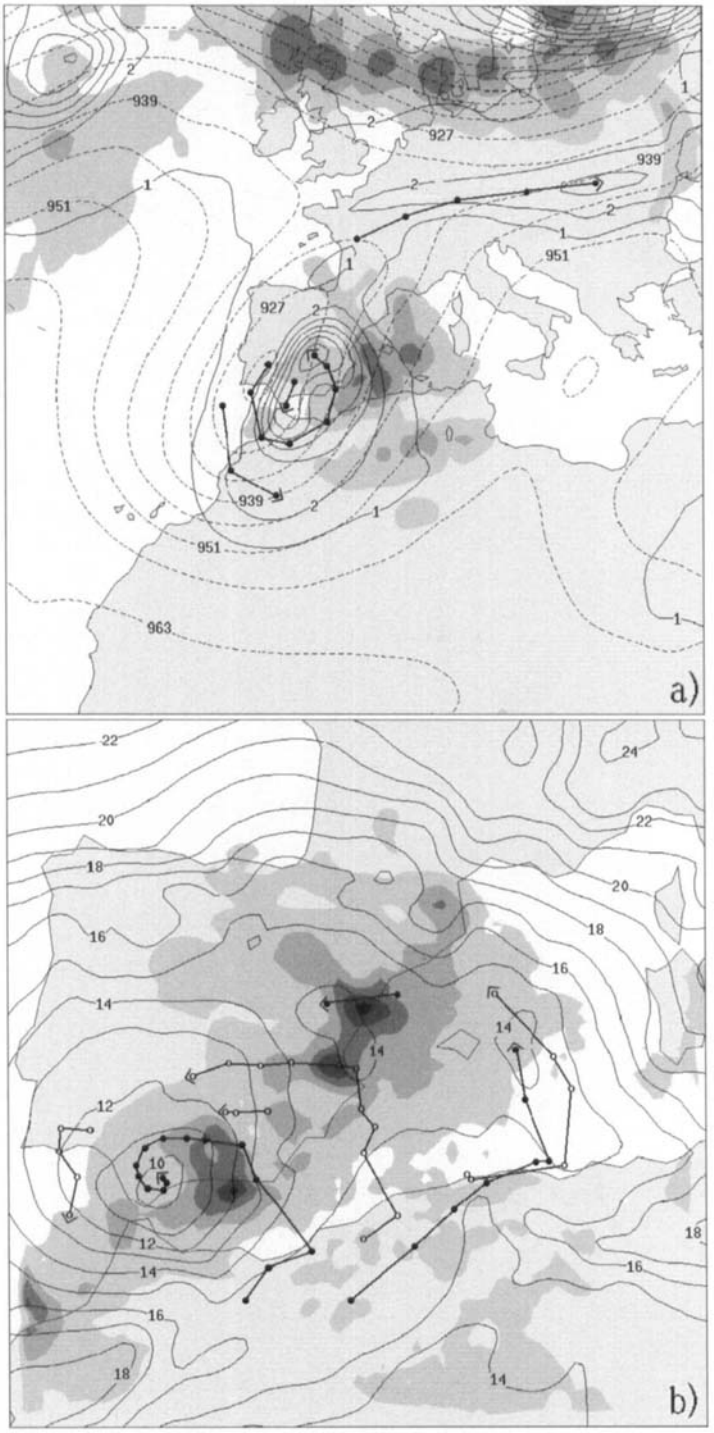

Figure 14. As Fig. 4, but for experiment S_{-}^{-}.

a weaker, slow-evolving situation, not very different from the basic experiment S_0^0. Dynamic forcing for upward motion is not very strong at any level over the area of interest. The surface disturbance and associated precipitation activity are quite stationary and restricted to the southern Mediterranean near the Algerian coast, very similar to the result of experiment S_0^0 (see Figs. 15(b) and 9(b)).

The effect of moving only the NE PV anomaly inward (experiment $S_{=}^{-}$) produces a geopotential-height wave resembling the previous case, S_{-}^{-}, except that the geopotential minimum is farther north (Fig. 16(a)). The evolution of the upper-level PV field is similar in both cases, although dynamic forcing for upward motion from those levels is somewhat weaker in the present case, owing to the smaller magnitude of the PV centre (compare Figs. 16(a) and 14(a)). In contrast, the low-level forcing induced by the warm air advection is similar in these cases, both in spatial distribution and intensity. Then, as expected from these considerations, the forecast surface pressure patterns and rainfall distributions are very similar in both situations (compare Figs. 16(b) and 14(b)).

When the above scenario is modified by moving the SW PV anomaly outward (experiment S_{+}^{-}; not shown), the upper-level PV field recovers a structure of two centres, and the evolution of the PV field around the Iberian peninsula is different. However, the pattern of low-tropospheric warm advection and its evolution is similar in both cases. The resulting surface disturbance and precipitation field are generally less intense but relatively similar in spatial pattern to the previous case $S_{=}^{-}$.

Even though experiment $S_{-}^{=}$ (not shown) appears to produce an upper-level trough significantly different than $S_{=}^{-}$ (in particular, a structure with two lows becomes evident), the evolution of the PV field upstream of the western Mediterranean is similar, as well as the structure and intensity of the low-tropospheric warm advection. Consequently, the evolution at the surface is similar in both cases, though in the present case the main low pressure centre and the rainfall along the Spanish coast are somewhat stronger.

When the SW PV anomaly is moved towards the Iberian peninsula but the NE PV anomaly is moved away (experiment S_{-}^{+}; not shown), the results do not differ significantly from the previous case $S_{-}^{=}$. The structure and evolution of both the upper-level PV field and the low-tropospheric pattern of warm advection are similar in both cases. The centre of the surface disturbance now appears displaced more towards south-eastern Spain, but the precipitation developed during the episode is quite similar.

Observe that all the previous experiments designed to study the impact of the position of the anomalies, with the exception of S_{+}^{+} in which the anomalies are largely decoupled, produce very similar results. The structure and track of the surface disturbance differ slightly among the experiments, but the precipitation field appears to be relatively insensitive to the position of the anomalies and quite similar to the control forecast. It would appear that changes in the position of the PV anomalies as here defined have generally little impact on the forecast. However, such generalizations are inadvisable for nonlinear problems; consider the results of experiment $S_{+}^{=}$ (Fig. 17). In this case, the evolution of dynamic forcing at all tropospheric levels is qualitatively different from the previous experiments (compare for example the pattern of warm advection at low levels). This results in a different surface pressure pattern, with the minimum now located near the Catalonia coast, and the precipitation signature is also substantially different (Fig. 17(b)). Curiously, this forecast turns out to be very similar to the results of experiment S_0^1 in section 2 (compare Figs. 17(b) and 12(b)). This is a consequence of both experiments having similar initial large-scale flow patterns upstream of the Mediterranean, in one case realized by removing the SW PV anomaly, and in the other case by moving it away from the region of interest.

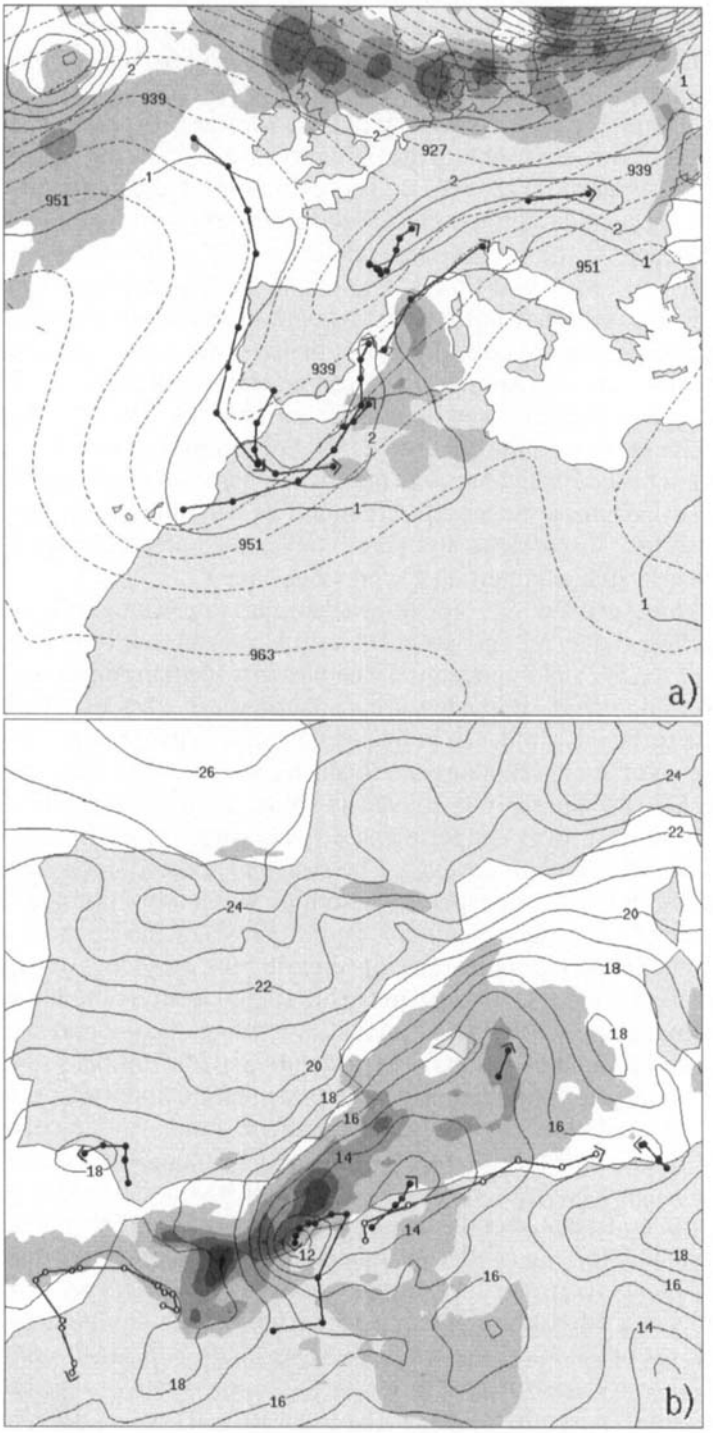

Figure 15. As Fig. 4, but for experiment S_{+}^{+}.

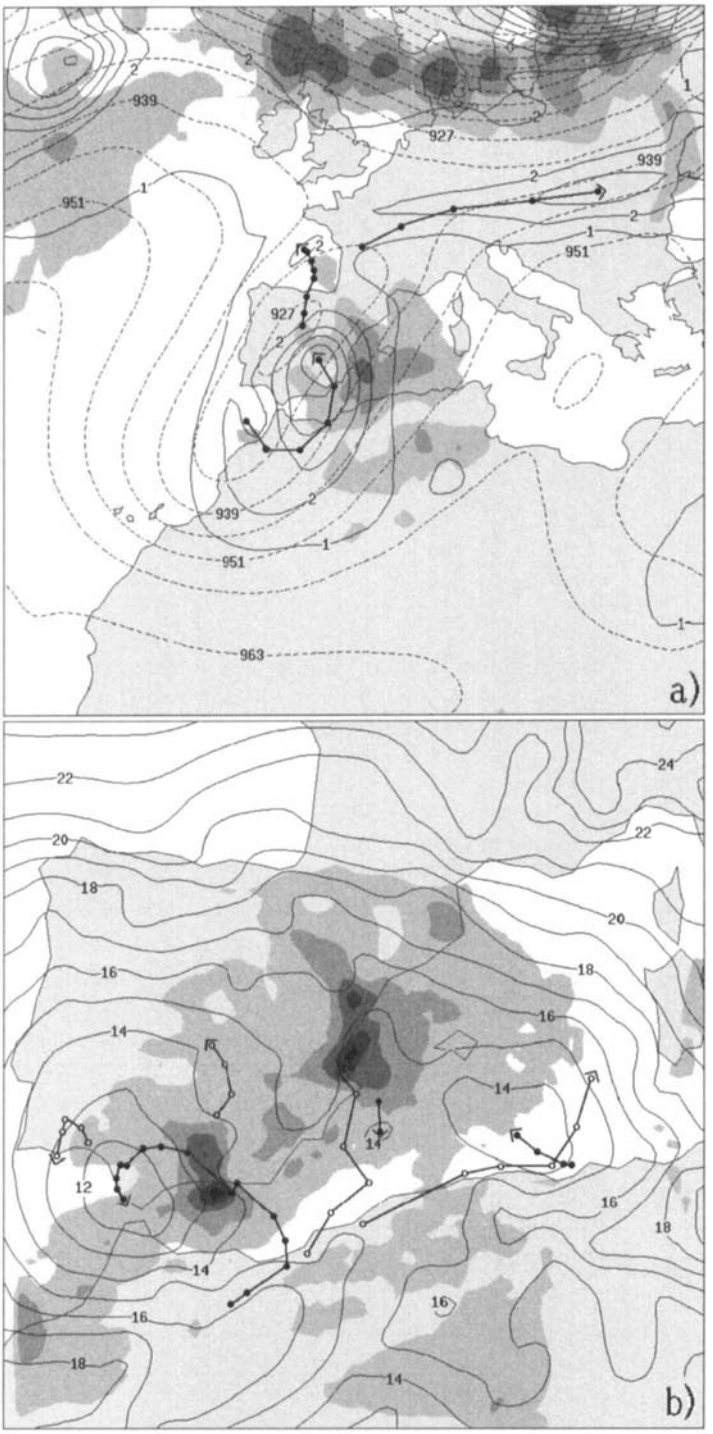

Figure 16. As Fig. 4, but for experiment $S_{=}^{-}$.

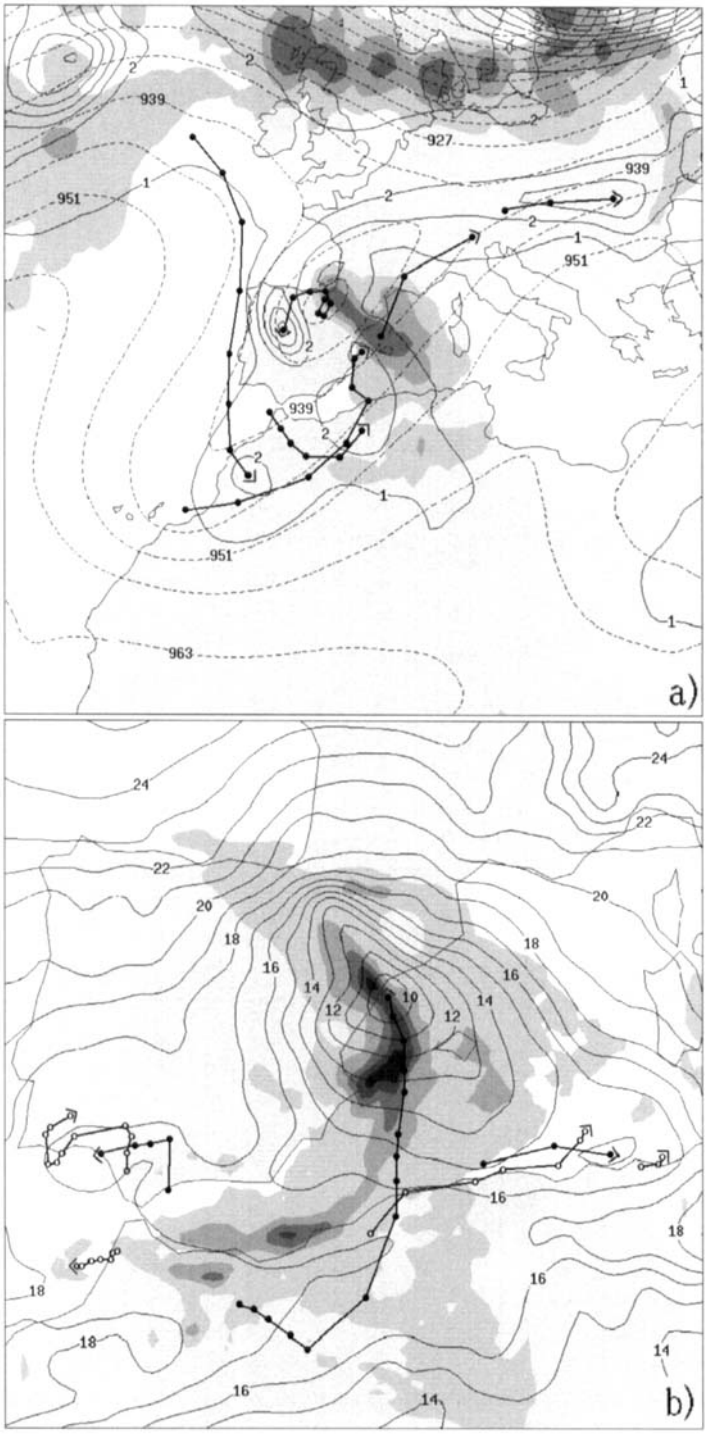

Figure 17. As Fig. 4, but for experiment $S_{+}^{=}$.

Finally, in experiment $S_{=}^{+}$ (Fig. 18), the model forecast again departs significantly from most of the previous simulations, but it shares many similarities with experiment S_{+}^{+}. For example, the shape and position of the predicted surface low pressure area (rather stationary in both scenarios) and the general structure of the induced precipitation, although in the present case these fields appear more displaced toward the northwest (compare Figs. 18(b) and 15(b)). As expected, the structure and evolution of the large-scale flow is not very different (Figs. 18(a) and 15(a)), but quasi-geostrophic forcing for upward motion is somewhat stronger at all tropospheric levels in the present case (not shown).

(*d*) *Discussion*

Focusing on the gross features of the flow only, the previous sensitivity experiments appear to embrace three main situations. The *first group*, consisting of experiments with the anomalies removed or moved away from each other (S_0^0, S_1^0, S_{+}^{+} and $S_{=}^{+}$) result in synoptically weak scenarios, characterized by stationary surface lows extended along the lee of the Atlas mountains and with most of the rainfall restricted to the southern Mediterranean areas. At the other extreme, a *second group* of experiments with enhanced PV structures aloft (S_2^2, S_{-}^{-}, $S_{=}^{-}$ and $S_{-}^{=}$) results in extensive and very mobile surface disturbances that also generate heavy rain in the northern Mediterranean zones. And the *third group*, in which the relative weight of the northern anomaly is enhanced (S_0^1, S_0^2, S_1^2 and $S_{+}^{=}$) tends to produce cyclones that evolve farther east and north of south-east Spain, thus inducing a concentration of most of the rainfall in northern Mediterranean areas. Of the remaining five experiments, S_2^0 produces a surface low and rainfall resembling those in the first group, and the other four members (S_2^1, S_{+}^{-}, S_{-}^{+} and the control simulation S) would be classified in the second group.

On the other hand, it would be interesting to judge the relevance of the upper-level PV anomalies relative to the action of other non-internal factors traditionally assumed—and also proved—to be very important in the western Mediterranean flash flood situations, notably the orography and the sea-surface latent-heat flux. Note that for all the numerical experiments presented there is a tendency for low pressure developments in the lee of the Atlas mountains, as well as precipitation enhancement in the exposed areas of eastern Spain. This suggests that both local and remote orographies could also have played an important role in this case. On the other hand, the simulations reveal intense evaporation from the warm (~23 °C) Mediterranean waters during the episode (not shown). For comparison, the control experiment S and the basic experiment S_0^0 were repeated, but eliminating the previous boundary factors (Fig. 19). The first experiment (Fig. 19(a)) still develops a large cyclone, but less intense and more circular than in the full simulation (compare with Fig. 4(b)). Clearly, the effect of the Atlas mountains in modulating the mean-sea-level pressure field over the Mediterranean is considerable, which implies an enhancement of the impinging easterly moist flow. The general area of precipitation in this modified control experiment does not change strongly, but the amounts are reduced. The output of the modified S_0^0 experiment (Fig. 19(b)), to be compared with the results of Fig. 9(b), does not even contain any noticeable low pressure centre over the Mediterranean, and the produced precipitation is very weak. In conclusion, the external factors induced an appreciable modulation of the surface circulation and enhanced the efficiency of the system as a rainfall producer, but the cyclogenesis that took place over the southern Mediterranean and its progression to the north must be attributed mostly to the action of the upper-level PV anomalies.

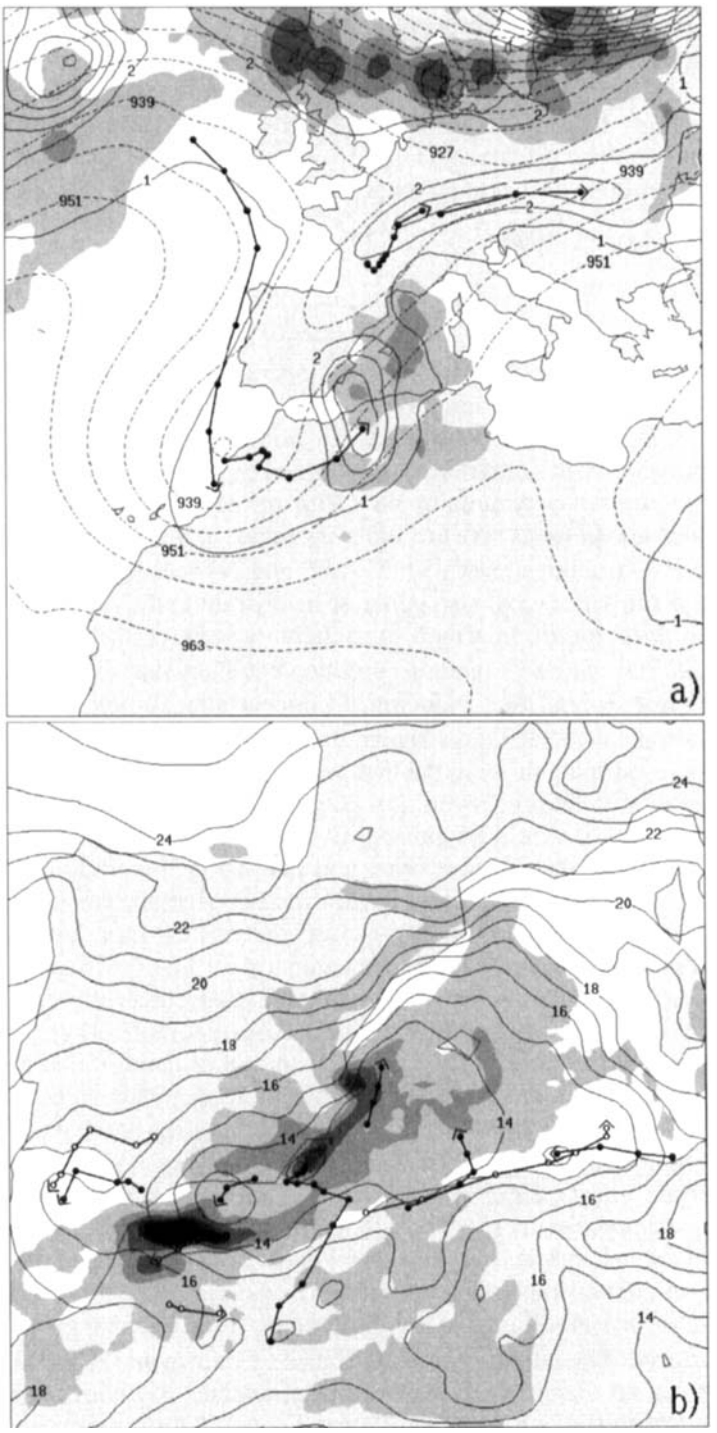

Figure 18. As Fig. 4, but for experiment $S_{=}^{+}$.

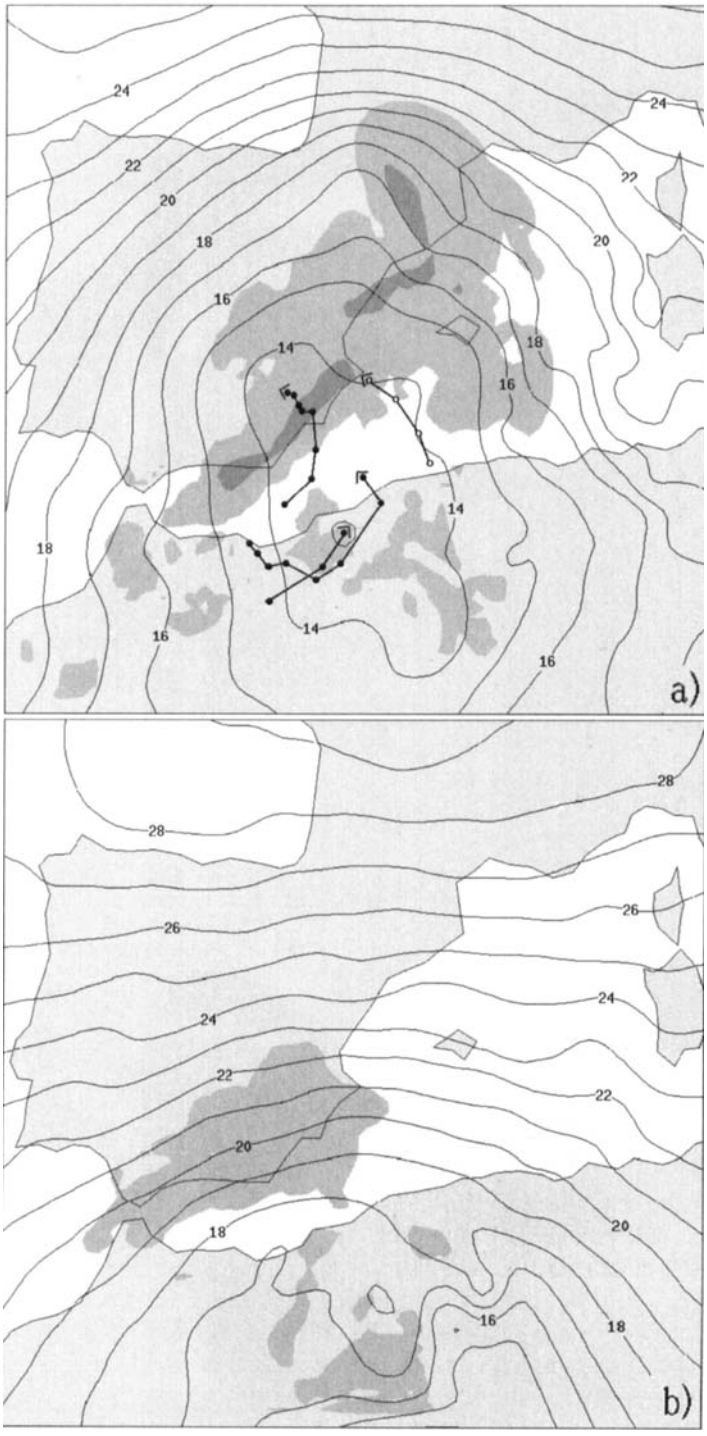

Figure 19. As Fig. 4(b), but for: (a) experiment S without orography and sea surface latent-heat flux; (b) experiment S_0^0 without orography and sea surface latent-heat flux.

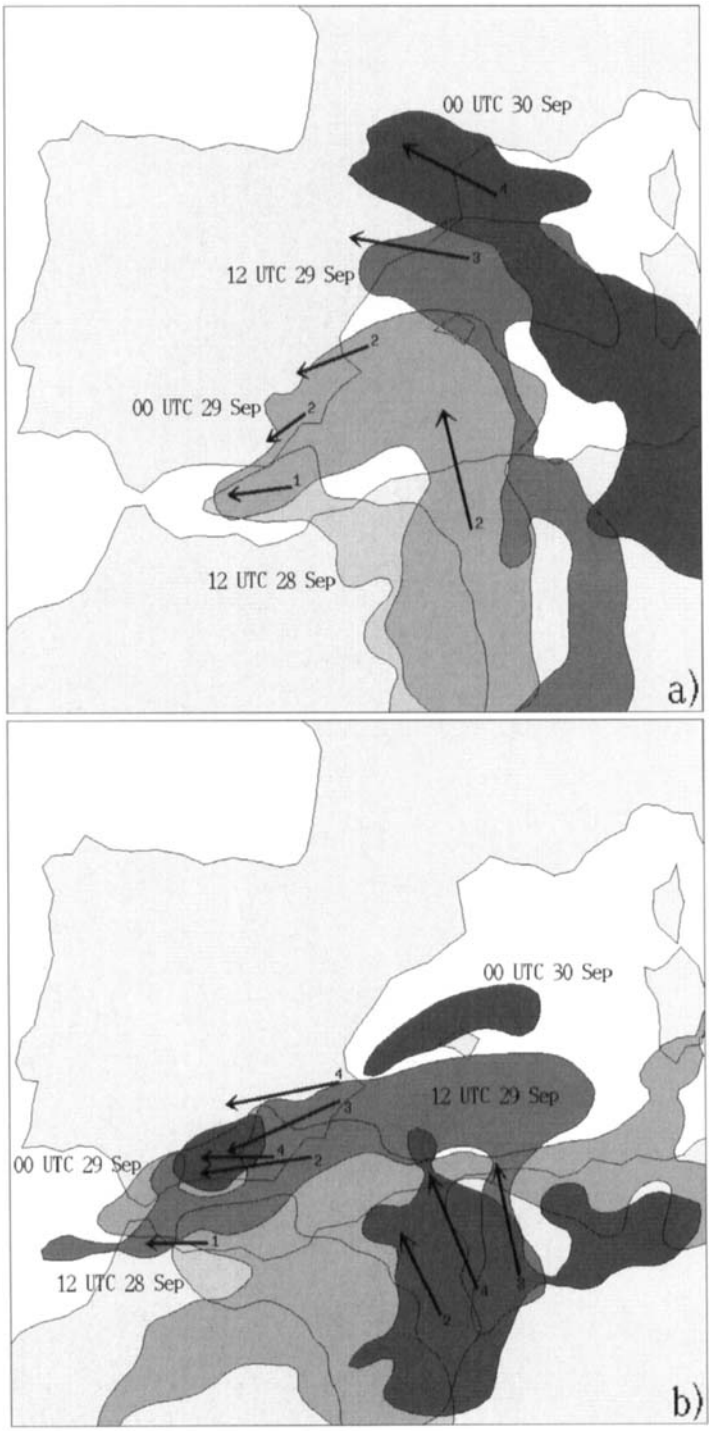

Figure 20. Time sequence showing, for the indicated times, zones with precipitable water greater than 40 mm (shaded) and the axis of low-level wind maxima (low-level jets, LLJs) as identified at 850 hPa (arrows): (a) experiment S, (b) experiment S_0^0, (c) experiment S_2^2, (d) experiment S_0^2. The LLJs are numbered in accordance with the four times shown.

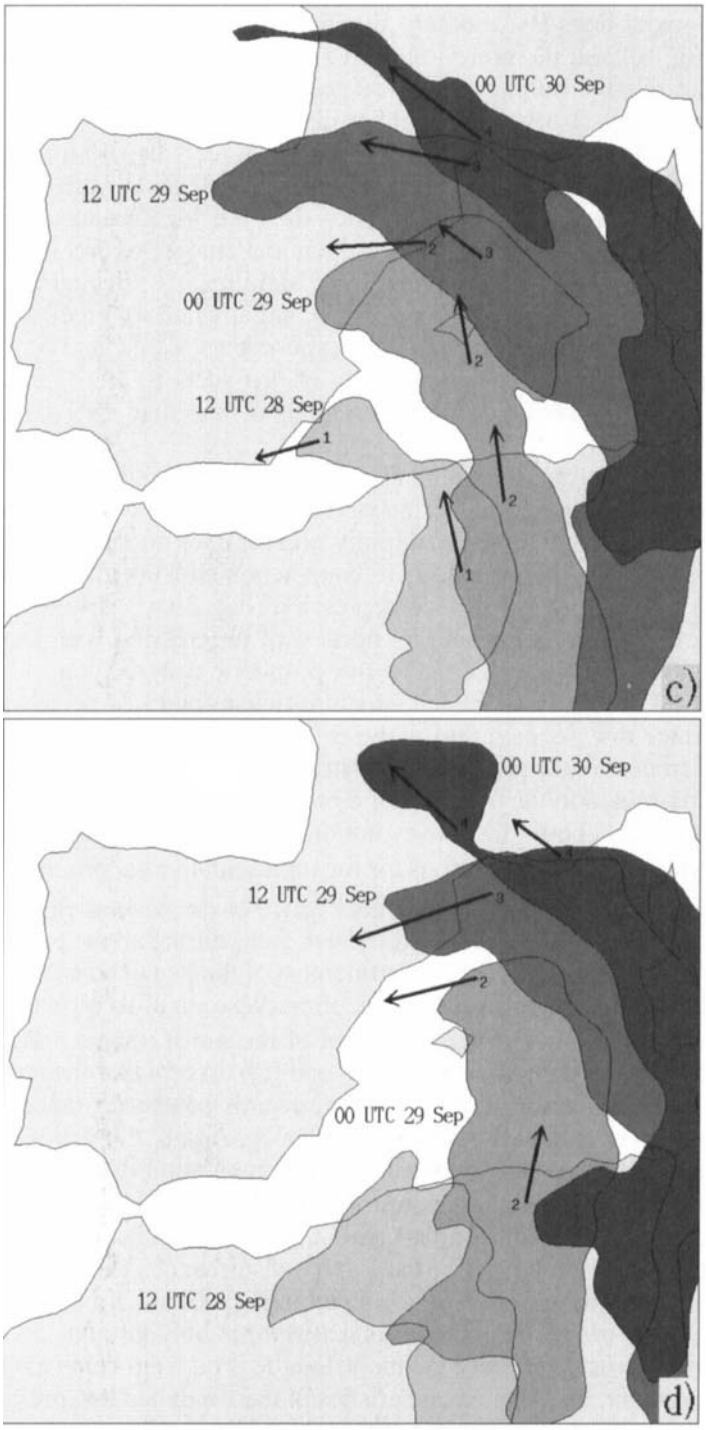

Figure 20. Continued.

Another interesting topic is the interrelation between dynamical and physical processes in connection with the heavy precipitation generation. Note that the addition or removal of an upper-level PV anomaly slightly modifies the near-surface stability and wind (recall Fig. 8), and therefore influences the initial values of the latent-heat flux. In addition, the relative humidity was left unchanged in the sensitivity experiments. Given the temperature changes, this implies changing the specific humidity among the different initial states. We argue that those initial aspects have only a secondary importance for both the spatial distribution and amounts of precipitation. First of all, the experiments exhibit similar evaporation rates over the Mediterranean during the first hours of simulation (not shown); secondly, the initial amount of precipitable water over the Mediterranean basin does not appear to be significantly affected by our simplistic treatment of the relative humidity. For example, initial values of precipitable water over the Balearic Islands for control run, S, and experiments S_0^0, S_2^2 and S_0^2 (representative of the three groups defined at the beginning of this section) are 27.8, 28.9, 26.4 and 26.9 mm, respectively. This represents variations of less than 10% between the most extreme values.

A close look at the control simulation outputs strongly suggests that the onset of heavy precipitation along the Mediterranean flank of Spain is associated with the intrusion of a well-defined moist tongue, initially present over north Africa but maintained by evaporation from the Mediterranean, in conjunction with the impinging easterly low-level jet (LLJ) induced by the surface depression (Fig. 20(a)). As expected, the combination of these two structures and its northward progression with time (Fig. 20(a)) is consistent with the evolution of the low-tropospheric water-vapour flux convergence pattern (displayed in Fig. 5). Since the moisture-rich air and LLJ occur to the north and east of the surface low, its path during the event is marked by the low characteristics. Therefore, differences in the precipitation distribution among the sensitivity experiments would be mostly rooted in the diversity of dynamical-forcing patterns noted in last section, which ultimately control the low evolution. This is shown by the time sequences of the moist tongue and the LLJ positions for the representative experiments S_0^0, S_2^2 and S_0^2 displayed in Figs. 20(b), (c) and (d), respectively. For the weak scenario S_0^0, the moist tongue remains over the southern Mediterranean areas during all the period, and the LLJ is also nearly stationary. This implies confinement of the heavy precipitation around the southern Mediterranean because of the lack of propagation of these features (Fig. 9(b)). The strong scenario S_2^2 leads to an evolution of the moist tongue and LLJ similar to the control experiment (compare Figs. 20(a) and (c)), except that these structures enter farther into inland Spain and progress faster towards southern France in response to the quicker and more extensive surface disturbance. Again, the genesis of heavy precipitation responds to the path followed by the combination of moist tongue and LLJ (Fig. 10(b)). Finally, for the third group of scenarios (represented by S_0^2; Fig. 20(d)), the moist tongue and LLJ evolve farther east and north of south-eastern Spain, owing to the aforementioned particularities of the surface disturbance. This implies a new mode of precipitation distribution, of the type shown in Fig. 13(b). Of course, the dynamical control of the heavy precipitation zones is realized not only through dry processes, but also through moist processes, since the moist tongue is far from being a purely advective property. In particular, once the characteristics of the simulated low pressure systems in the different scenarios start to diverge within the forecast period, the evaporation rates from the Mediterranean (especially intense in areas of strong surface winds) also differ among the different experiments. This affects, to some extent, the moisture distribution and thus the precipitation values.

4. CONCLUSIONS

The western Mediterranean cyclogenesis event of 28–29 September 1994 represents a very interesting situation, owing to the presence of two interacting and fast-evolving upper-level PV centres upstream of the region. The role of these PV centres in the surface evolution of the cyclone and the associated heavy rain has been numerically assessed using diagnostic products and a piecewise PV-inversion method in conjunction with mesoscale model simulations. This and previous case-studies have shown that the diagnosis of quasi-geostrophic dynamic forcing for upward motion, and not for other parameters, such as low-tropospheric water vapour flux convergence and convective instability, generally offer an accurate picture of the cyclone evolution and the development of deep, moist convection, especially when the analysis is combined with conceptual models of mesoscale interaction between the large-scale flow and the complex orography of the region. In this sense, an analysis of this type of event in terms of PV, or the so-called 'PV thinking' approach, is merely an alternative to the capabilities of the more traditional quasi-geostrophic theory.

However, the combined application of piecewise PV-inversion and numerical simulation offers a valuable framework from which the effects of dynamical features of the flow can be studied in a practical and physically consistent way. In this work, the approach was used to generate an ensemble of mesoscale numerical simulations with perturbed initial intensities or perturbed positions of the embedded upper-level PV centres. The set of hypothetical scenarios constructed in this way appears to be very useful for investigating the predictability of mesoscale details of the forecast, subject to potential errors in the initial representation of the upper-level disturbance. In this sense, the PV-based approach used in this and previous works (e.g. Fehlmann *et al.* 2000) is similar in scope to more classical adjoint techniques used in ensemble forecasting (e.g. Petrologis *et al.* 1996). However, they differ substantially from methodological considerations; note that we define perturbations based on selected finite-amplitude physical attributes of the precursor upper-level disturbance, but these features are not necessarily the most unstable aspects of the flow that an adjoint method would seek to determine.

The designed experiments clearly illustrate the importance of the two embedded upper-level PV anomalies as regards the track, shape and intensity of the surface cyclone and the corresponding rainfall pattern. Interestingly, more distinct behaviours were found with perturbed *intensities* of the anomalies than with perturbed *positions*, although this may in part be related to the arbitrariness involved in the definition of the perturbations. On the other hand, the mean-sea-level pressure pattern generally exhibited higher sensitivity to the perturbed anomalies than did the rainfall distribution, probably because precipitation generation is largely controlled, under easterly regimes, by the interaction of the moist flow with the coastal topographic features. This result suggests that the forecast of important surface parameters, such as the wind speed and direction, can sometimes be as critical as the forecast of the occurrence and amount of precipitation.

As expected, the effects on the forecasts observed after perturbing the initial structure of the upper-level disturbance could be directly explained in terms of the dynamic-forcing patterns associated with the evolution of the warm air advection and PV fields at low and mid-upper tropospheric levels, respectively. The resulting evolution of a well-defined Mediterranean moist tongue in combination with the onshore LLJ were shown to determine where and when, for each initial state, the heavy precipitation occurs. However, these effects could not easily be anticipated prior to the model runs, certainly as a consequence of the nonlinear nature of the problem.

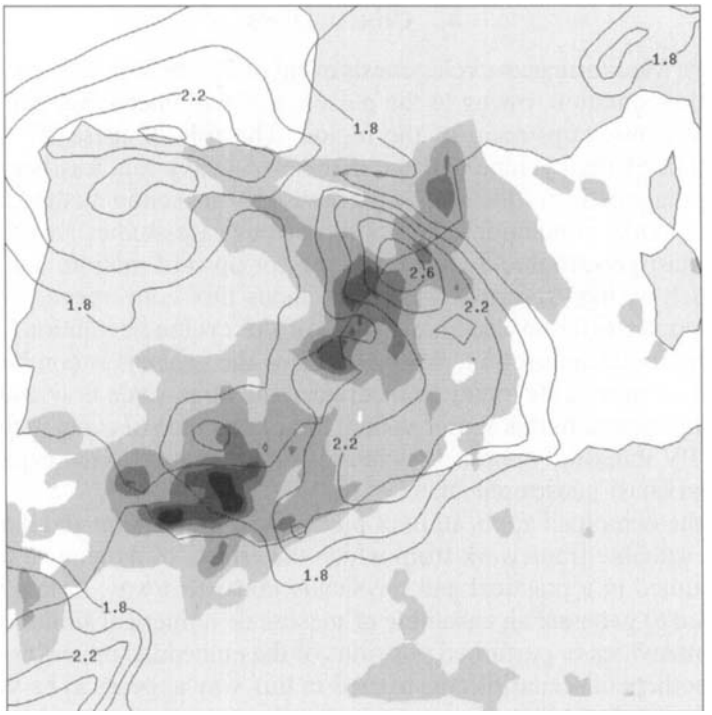

Figure 21. Standard deviations of the mean-sea-level pressure tendency during the forecast period (continuous line, in hPa/48 h starting at 1.8 hPa/48 h) and total precipitation (shaded, for values exceeding 10, 20, 30, 40 and 50 mm), calculated from the ensemble of 17 experiments performed.

A synthesis for our case-study in terms of predictability is presented in Fig. 21, which contains an evaluation of the pressure tendency and precipitation variability within the full ensemble of forecasts. With respect to the amount of surface pressure fall, the most sensitive area to the considered uncertainties of the upper-level PV field appears to be southern Catalonia, though the predictive skill would in general be limited in all the western half of the Mediterranean basin under such a source of error. Prediction of the approximate amounts of rainfall in the coastal regions of Spain would be equally difficult, especially near the Gulf of Valencia, in Andalucia and Catalonia. These results stress the importance of minimizing any error in the analysed initial structure of the synoptic-scale flow for the successful forecasts of mesoscale detail, and show the value of ensemble forecasting (Brooks *et al.* 1995) when uncertainties are likely in the representation of the atmosphere.

ACKNOWLEDGEMENTS

Constructive comments on an earlier version of this manuscript from Dr Charles Doswell III and Dr David Schultz helped to improve the content and presentation. I am also grateful to Dr Chris Davis for his guidance during the implementation of the PV-inversion method. The development of the study was supported by the Scientific Program of NATO for post-doctoral research at the National Severe Storms Laboratory. Computer support provided by NCAR/Scientific Computer Division (which is sponsored by the National Science Foundation) for model data preprocessing is also acknowledged. Precipitation and satellite data of the event were provided by the Spanish

Instituto Nacional de Meteorología (INM) and Professor J. L. Casanovas from the University de Valladolid, respectively.

REFERENCES

Benjamin, S. G. 1983 'Some effects of heating and topography on the regional severe storm environment'. PhD Thesis, The Pennsylvania State University

Benjamin, S. B. and Seaman, N. L. 1985 A simple scheme for improved objective analysis in curved flow. *Mon. Weather Rev.*, **113,** 1184–1198

Betts, A. K. 1986 A new convective adjustment scheme. Part I: Observational and theoretical basis. *Q. J. R. Meteorol. Soc.*, **112,** 677–692

Betts, A. K. and Miller, M. J. 1986 A new convective adjustment scheme. Part II: Single column tests using GATE wave, BOMEX, ATEX and Arctic air-mass datasets. *Q. J. R. Meteorol. Soc.*, **112,** 693–709

Binder, P. and Schär, C. 1998 'The MAP design proposal'. Available from MAP Programme Office, Swiss Meteorological Institute, Krähbühlstrasse 58, Postfach, 8044 Zürich, Switzerland

Blackadar, A. K. 1979 High resolution models of the planetary boundary layer. Pp. 50–85 in *Advances in environmental science and engineering*, Volume 1, No. 1. Eds. J. Pfafflin and E. Ziegler. Gordon and Breach, Newark, NJ 07102, USA

Brooks, H. E., Tracton, M. S., Stensrud, D. J., DiMego, G. and Toth, Z. 1995 Short-range ensemble forecasting: Report from a workshop (25–27 July 1994). *Bull. Am. Meteorol. Soc.*, **76,** 1617–1624

Buzzi, A., Tartaglione, N. and Malguzzi, P. 1998 Numerical simulations of the 1994 Piedmont flood. Role of orography and moist processes. *Mon. Weather Rev.*, **126,** 2369–2383

Charney, J. G. 1955 The use of primitive equations of motion in numerical prediction. *Tellus*, **7,** 22–26

Davis, C. A. 1992a A potential-vorticity diagnosis of the importance of initial structure and condensational heating in observed extratropical cyclogenesis. *Mon. Weather Rev.*, **120,** 2409–2428

1992b Piecewise potential vorticity inversion. *J. Atmos. Sci.*, **49,** 1397–1411

Davis, C. A. and Emanuel, K. A. 1991 Potential vorticity diagnostics of cyclogenesis. *Mon. Weather Rev.*, **119,** 1929–1953

Doswell, C. A. III 1987 The distinction between large-scale and mesoscale contribution to severe convection: A case study example. *Weather and Forecasting*, **2,** 3–16

Doswell, C. A. III, Brooks, H. E. and Maddox, R. A. 1996 Flash flood forecasting: An ingredients-based methodology. *Weather and Forecasting*, **10,** 560–581

Doswell, C. A. III, Ramis, C., Romero, R. and Alonso, S. 1998 A diagnostic study of three heavy precipitation episodes in the western Mediterranean region. *Weather and Forecasting*, **13,** 102–124

Dudhia, J. 1989 Numerical study of convection observed during the winter monsoon experiment using a mesoscale two-dimensional model. *J. Atmos. Sci.*, **46,** 3077–3107

1993 A nonhydrostatic version of the Penn State/NCAR mesoscale model: Validation tests and simulation of an Atlantic cyclone and cold front. *Mon. Weather Rev.*, **121,** 1493–1513

Ertel, H. 1942 Ein neuer hydrodynamischer wirbelsatz. *Meteorologishe Zeitschrift*, **59,** 271–281

Fehlmann, R. and Davies, H. C. 1999 Role of salient PV-elements in an event of frontal wave cyclogenesis. *Q. J. R. Meteorol. Soc.*, **125,** 1801–1824

Fehlmann, R., Quadri, C. and Davies, H. C. 2000 An Alpine rainstorm: Sensitivity to the mesoscale upper-level structure. *Weather and Forecasting*, **15,** 4–28

Fernández, C., Gaertner, M. A., Gallardo, C. and Castro, M. 1995 Simulation of a long-lived meso-β scale convective system over the mediterranean coast of Spain. Part I: Numerical predictability. *Meteorol. Atmos. Phys.*, **56,** 157–179

1997 Simulation of a long-lived meso-β scale convective system over the mediterranean coast of Spain. Part II: Sensitivity to external forcings. *Meteorol. Atmos. Phys.*, **62,** 179–200

García-Dana, F., Font, R. and Rivera, A. 1982 'Situación meteorológica durante el episodio de lluvia intensa en el levante español durante Octubre de 1982'. Available from: Instituto Nacional de Meteorología, Apartado 285, E-28071 Madrid, Spain (in Spanish)

Grell, G. A., Dudhia, J. and Stauffer, D. R. 1995 'A description of the fifth-generation Penn State/NCAR mesoscale model (MM5)'. NCAR Tech. Note NCAR/TN–398+STR

Hakim, G. H., Keyser, D. and Bosart, L. F. 1996 The Ohio valley wave-merger cyclogenesis event of 25–26 January 1978. Part II: Diagnosis using quasi-geostrophic potential vorticity inversion. *Mon. Weather Rev.*, **124**, 2176–2205

Homar, V., Ramis, C., Romero, R., Alonso, S., García Moya, J. A. and Alarcón, M. 1999 A case of convection development over the western Mediterranean Sea: A study through numerical simulations. *Meteorol. Atmos. Phys.*, **71**, 169–188

Hoskins, B. J. and Pedder, M. A. 1980 The diagnosis of middle latitude synoptic development. *Q. J. R. Meteorol. Soc.*, **106**, 707–719

Hoskins, B. J., McIntyre, M. E. and Robertson, A. W. 1985 On the use and significance of isentropic potential-vorticity maps. *Q. J. R. Meteorol. Soc.*, **111**, 877–946

Huo, Z., Zhang, D. L. and Gyakum, J. R. 1998 An application of potential vorticity inversion to improving the numerical prediction of the March 1993 Superstorm. *Mon. Weather Rev.*, **126**, 424–436

1999a Interaction of potential vorticity anomalies in extratropical cyclogenesis. Part I: Static piecewise inversion. *Mon. Weather Rev.*, **127**, 2546–2561

Huo, Z., Zhang, D. L. and Gyakum, J. R. 1999b Interaction of potential vorticity anomalies in extratropical cyclogenesis. Part II: Sensitivity to initial perturbations. *Mon. Weather Rev.*, **127**, 2563–2575

Kain, J. S. and Fritsch, J. M. 1990 A one-dimensional entraining/detraining plume model and its application in convective parameterization. *J. Atmos. Sci.*, **47**, 2784–2802

Lionetti, M. 1996 The Italian floods of 4–6 November 1994. *Weather*, **51**, 18–27

Meteorological Office 1962 *Weather in the Mediterranean*. Vol. 1, HMSO, London, UK

Morgan, M. C. 1999 Using piecewise potential vorticity inversion to diagnose frontogenesis. Part I: Partitioning of the Q vector applied to diagnosing surface frontogenesis and vertical motion. *Mon. Weather Rev.*, **127**, 2796–2821

Petrologis, T., Buizza, R., Lanzinger, A. and Palmer, T. N. 1996 Extreme rainfall prediction using the European Centre for Medium-Range Weather Forecasts ensemble prediction system. *J. Geophys. Res.*, **101**, (D21), 26227–26236

Ramis, C. 1995 Las observaciones de la atmósfera libre en Mallorca: una breve historia y algunos resultados. *Revista de Ciència*, **17**, 41–58

Ramis, C., Llasat, M. C., Genovés, A. and Jansá, A. 1994 The October 1987 floods in Catalonia: Synoptic and mesoscale mechanisms. *Meteorol. Appl.*, **1**, 337–350

Ramis, C., Romero, R., Homar, V., Alonso, S. and Alarcón, M. 1998 Diagnosis and numerical simulation of a torrential precipitation event in Catalonia (Spain). *Meteorol. Atmos. Phys.*, **69**, 1–21

Riosalido, R. 1990 'Characterization of mesoscale convective systems by satellite pictures during PREVIMET MEDITERRANEO-89'. Pp. 135–148 in Segundo Simposio Nacional de Predicción. Instituto Nacional de Meteorología, Apartado 285, 28071, Madrid, Spain (in Spanish)

Riosalido, R., Rivera, A. and Martín, F. 1988 'Development of a mesoscale convective system in the Spanish Mediterranean area'. Pp. 375–378 in preprints of the seventh Meteosat scientific users' meeting, Madrid. EUMETSAT, Darmstadt, Germany

Romero, R., Doswell, C. A. III and Ramis, C. 2000 Mesoscale numerical study of two cases of long-lived quasistationary convective systems over eastern Spain. *Mon. Weather Rev.*, **128**, 3731–3751

Rossby, C. G. 1940 Planetary flow patterns in the atmosphere. *Q. J. R. Meteorol. Soc.*, **66**, 68–87

Sénési, S., Bougeault, P., Cheze, J. L., Cosentino, P. and Thépenier, R. M. 1996 The Vaison-la-Romaine flash flood: Meso-scale analysis and predictability issues. *Weather and Forecasting*, **11**, 417–442

Stein, U. and Alpert, P. 1993 Factor separation in numerical simulations. *J. Atmos. Sci.*, **50**, 2107–2115

Washington, W. M. and Baumhefner, D. P. 1975 A method of removing Lamb waves from initial data for primitive equation models. *J. Appl. Meteorol.*, **14**, 114–119

Wheeler, D. 1995 Heavy rainfall in Catalonia, October 1994. *Weather*, **50**, 362–367

Zhang, D. L. 1989 The effect of parameterized ice microphysics on the simulation of vortex circulation with a mesoscale hydrostatic model. *Tellus*, **41A**, 132–147

Zhang, D. L. and Anthes, R. A. 1982 A high-resolution model of the planetary boundary layer. Sensitivity tests and comparisons with SESAME-79 data. *J. Appl. Meteorol.*, **21**, 1594–1609

Zhang, D. L. and Fritsch, J. M. 1986 Numerical simulation of the meso-β scale structure and evolution of the 1977 Johnstown flood. Part I: Model description and verification. *J. Atmos. Sci.*, **43**, 1913–1943

Zhang, D. L., Chang, H. R., Seaman, N. L., Warner, T. T. and Fritsch, J. M. 1986 A two-way interactive nesting procedure with variable terrain resolution. *Mon. Weather Rev.*, **114**, 1330–1339